J. Webster (ed.), *Wiley Encyclopedia of Electrical and Electronics Engineering*

MICROSTRIP ANTENNAS

Microstrip circuitry consists of a metal strip or patch on a dielectric substrate backed by a metal ground plane. Microstrip antennas are becoming increasingly popular owing to their advantages in size, cost, conformity to the supporting structure, low profile, and ease of fabrication. By using simple etching techniques, it is possible to fabricate a wide variety of microstrip circuits, including arrays of antennas, feeding networks, and active devices such that preamps or distributed transmitters can be conveniently placed next to the antenna elements. In addition, diode phase shifter circuits can also be etched on the substrate to form single-board phased arrays. This article describes the microwave properties of patch antennas.

The dimensions of microstrip patch antennas are large in comparison with the width of conventional microstrip lines. The ma purpose of a patch antenna is to confine microwave energy to a small finite region. Such confinement may be achieved with the resonant behavior of a finite guided structure supporting standing modes. Electromagnetic energy radiates from that part of the patch that is open to free space, similar to a slot cut along the side of a waveguide. To continuously radiate microwave energy away, the patch needs to be electrically connected to a so-called feeder line. When the characteristic impedance of the feeder line matches the impedance of radiation waves, power is directly dumped into the confined space of the patch without causing much reflection. This means that all of the input power to the patch is radiated away into free space. A conventional transmission line radiates little power, because the fringing fields alternate in sign over a short distance, resulting in cancellation of their radiated field. In microstrip circuitry, power also radiates from open circuits and from discontinuities, such as corners. The radiated power is small, however, because the radiation impedances there are usually much higher than the characteristic impedance of the microstrip transmission line encompassing these discontinuities.

This article introduces two calculation methods capable of describing antenna performance quantitatively. The first method is less rigorous, but it has the advantage of being more analytical and hence can be applied with ease. Called the resonant cavity model, it assumes perfect metal boundaries at the metal patch and ground plane and magnetic-wall boundary conditions at the periphery, or sides of the patch antenna. It is well known, that there are fringing fields at the periphery of the patch antenna. The influence of such fields may be included in this approximate analysis by extending the linear dimension of the patch antenna by a small amount consistent with the depth of the fringing fields. Radiation and material imperfections are then considered as perturbations to the lossless cavity. As such, the resonant frequency, far-field pattern, input impedance, radiation linewidth, and efficiency are all calculable. The only shortcoming of this simple cavity model is that it is not able to address the possibility of the propagation of surface waves. Surface wave generation becomes significant in comparison with patch radiation for a thick substrate with high dielectric constant.

The second calculation method concerns Green's function analysis. In general, a Green's function is defined as the solution of a differential or integral equation resulting from a (delta-function) point source satisfying the required (hogeneous) boundary conditions. Thus, under arbitrary source excitation, the solutn of the equation can be obtained by a superposition ofreen's functions, still satisfying the boundary conditions. In the presence of a point (dipole) current source in the background of a stratified structure consisting of dielectric or magnetic

layers, the excited electromagnetic field is termed a dyadic Green's function from the vectorial nature of the source field and the observer field. Although the construction of the dyadic Green's function is straightforward, this article pays special attention to its physical interpretations as it appeared in the original work by 1.

Actually, Sommerfeld solved for the first time the Green's functions associated with a horizontal point dipole and a vertical point dipole in the presence of a semiinfinite conductor half-space: the Earth (1). Radio waves are radiated into free space either directly from the point dipole source or indirectly from the image dipole source induced by the (imperfect) ground plane, the Earth's surface. These are called spatial waves, because they exhibit a $1/r$ spatial dependence, where r denotes the distance from the original source point (or image point) to the observer point. However, Sommerfeld also showed a second kind of radiation field, which is tied to the air–earth interface exhibiting a $1/\sqrt{\rho}$ dependence, where ρ denotes the 2-D distance between the source point projected on the Earth's surface to the observer point located also on the Earth's surface (1). They are called surface waves, because they decay exponentially when departing away from the air–earth interface. This article explains how the spatial wave solutions and the surface wave solutions are constructed from a (horizontal) point dipole source in the presence of a layered dielectric or magnetic structure.

By using the dyadic Green's function, the general field solution in a stratified structure with external current excitation can then be formulated in terms of an integral equation, which is subsequently solved by applying the numerical Galerkin method. This article outlines procedures to calculate engineering parameters of general microstrip antennas and gives calculation results for circular microstrip antennas, including radiation frequencies, bandwidths, far-field patterns, input impedances, effects of feeder-line position, and interference between antennas. Recent developments on printed-circuit antennas are briefly reviewed, including the important broadband technique employing stacked parasitic elements to achieve high gain and low cross-polarization levels. More sophisticated treatments on microstrip antennas may be found in Ref. 2.

Cavity Model

A microstrip patch antenna is a narrow-band device, and typically, the bandwidth covers approximately 5 percent of the radiation frequency. When the bandwidth, Δf, can be related to the Q of a resonator

$$Q = 2\pi f \left(\frac{\text{maximum stored energy}}{\text{averaged power dissipation}} \right) = \frac{f}{\Delta f} \qquad (1)$$

it implies that power dissipation is not significant and the circuit of a microstrip patch antenna can be approximated as a low-loss cavity resonator. This suggests that the performance of a microstrip patch antenna can be analyzed using a perturbation method. That is, the zeroth order solution of the antenna is described in terms of the eigen modes, or normal modes, of a lossless cavity. Losses are then added to the analysis as first-order perturbations, including conductor loss, dielectric loss, and radiation loss. Magnetic loss can also be included in the total loss if ferrites are used as the substrate material.

Analogous to radiation loss, surface wave loss may also be treated as a perturbation in the cavity model. Radiation and surface wave losses may be represented as leaky waves from the antenna, the former directly from air and the latter from the guided structure of the substrate. However, the analysis of surface-wave loss may be difficult, because it involves Sommerfeld-type integrals where simple poles and branch cuts appear in the complex k plane (1). Usually, surface waves are included only in a full-wave analysis in which Maxwell equations are solved numerically in the microstrip geometry.

In contrast, the cavity model is easier to apply, allowing engineering parameters of a microstrip patch antenna to be calculated analytically, including bandwidth, input impedance, radiation efficiency, and near-field and far-field patterns. Furthermore, the physical meaning of normal modes is evident in the cavity

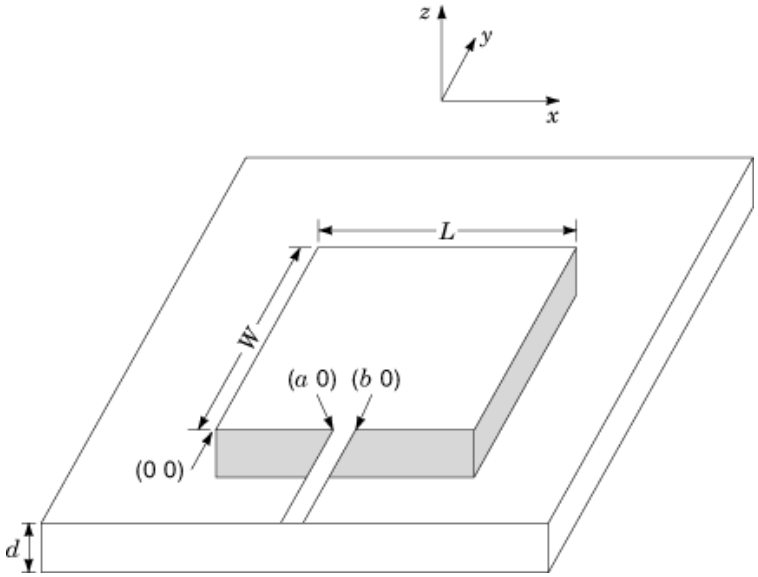

Fig. 1. Feeding the rectangular patch antenna by a microstrip line. The resonant cavity locates directly under the patch bound by a magnetic wall, shown shaded in the figure.

model. For example, the left- or right-hand polarized radiation from a microstrip ferrite patch antenna can be readily calculated by using the cavity model. The cavity model provides satisfactory quantitative answers if surface wave losses are minimal. Surface wave losses are minimal for a thin substrate exhibiting low dielectric constant, but not for a thick substrate with high dielectric constant. Also, for microstrip patches in proximity to each other a full-wave analysis is required, since the cavity model is not sufficient to describe these complex situations. The full-wave analysis involving the use of dyadic Green's functions is discussed later.

Resonant Frequency. Let a metal patch be deposited on top of a dielectric substrate backed by a ground plane. The patch considered here is either of rectangular or circular geometry. Only dielectric substrates are considered. Analysis of patch antennas with ferrite substrates may be found in Ref. 3. In the cavity model one assumes a lossless substrate in which the cavity is bounded by an electric and a magnetic wall. The metal surfaces of the microstrip patch and the ground plane may be approximated as perfect conductors or electric walls, but the peripheral surface surrounding the antenna cavity directly under the patch is assumed to be a magnetic wall. This is illustrated in Fig. 1, in which a microstrip rectangular patch antenna is represented by a cavity with its periphery shown shaded as a magnetic wall. An electric or magnetic wall is defined such that the tangential component of the electric or magnetic field vanishes at the wall boundary. Thus, a normal metal boundary condition approaches that of an electric wall if the value of conductivity goes to infinity. A magnetic wall imposes imaginary boundary conditions that insulate the inside of the cavity from the outside, allowing no electromagnetic energy to propagate across it.

Under quasi-static assumptions a magnetic wall can be located at the periphery of a patch antenna, provided that it encloses the total volume of the antenna plus its fringing fields. That is, the effective volume of the cavity is slightly larger than the physical one, so that it accounts for both the electromagnetic energy stored directly under the metal patch and its fringe. This is shown in Fig. 2, for the case of a circular microstrip antenna, where the effective radius of the cavity is larger than that of the metal patch. Thus, the resonant length at the side of a rectangular patch antenna, denoted as $L' = L + 2\Delta$, is larger than the physical length,

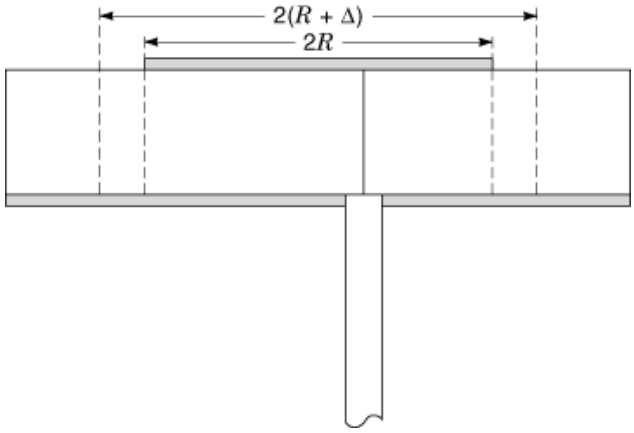

Fig. 2. Feeding the circular patch antenna by a coax line. Due to the fringing-field effect the effective radius of the resonator is larger than its physical value.

L, and the effective increment in length due to the fringing-field effect (4) is 2Δ with

$$\frac{\Delta}{d} = 0.412\left(\frac{\epsilon_{\text{eff}} + 0.300}{\epsilon_{\text{eff}} - 0.258}\right)\left(\frac{L/d + 0.262}{L/d + 0.813}\right) \tag{2}$$

where d is the thickness of the substrate, ϵ_{eff} denotes the effective dielectric constant of the patch cavity (5) given by

$$\epsilon_{\text{eff}} = \frac{\epsilon_{\text{r}} + 1}{2} + \frac{\epsilon_{\text{r}} - 1}{2}\left(1 - \frac{10d}{L}\right)^{-1/2} \tag{3}$$

and ϵ_{r} is the dielectric constant of the substrate material. The rationale behind Eq. (3) is that, depending on the ratio of d/L, electric field lines can still propagate away from the cavity region, and so $\epsilon_{\text{eff}} < \epsilon_{\text{r}}$, and $\epsilon_{\text{eff}} \approx \epsilon_{\text{r}}$ if $d/L \ll 1$. The resonant frequency of the cavity resonator is therefore

$$f_n = \frac{cn}{2L'\sqrt{\epsilon_{\text{eff}}}} \tag{4}$$

where c denotes the speed of light in vacuum and n the order of the resonant mode ($n = 1$ for the fundamental mode).

Based on the same fringing-field consideration, we expect that for a circular patch antenna the effective resonant radius of the cavity, denoted as $R' = R + \Delta$, is larger than the physical radius of the metal patch (6), denoted as R, and

$$\Delta = \frac{d}{\pi}\left[\ln\left(\frac{\pi R}{2d}\right) + 1.7726\right] \tag{5}$$

as shown in Fig. 2. A similar expression for ϵ_{eff} as Eq. (3) is expected for a circular microstrip cavity. However, such an expression is lacking in the present literature. We therefore use the value of ϵ_{r} for ϵ_{eff}, bearing in mind

that this approximation is true only when $R \gg d$. The resonant frequency of the cavity is, therefore

$$f_{mn} = \frac{cX'_{mn}}{2\pi R'\sqrt{\epsilon_r}} \tag{6}$$

where X'_{mn} is the nth zero of the derivative of the Bessel function $J_m(x)$ of order m.

We note that the above expressions for resonant frequencies for rectangular and circular microstrip patch antennas [Eqs. (4) and (6)] are derived based on the cavity model according to which standing modes are excited within the cavity. At high frequencies the quasi-static assumption is no longer valid, and surface waves of high orders are generated and propagating away from the cavity region guided by the dielectric substrate. In this case, magnetic-wall boundary conditions are not appropriate at the periphery of the antenna cavity. For these situations we must resort to a rigorous full-wave analysis to adequately address the leaky feature of surface waves—for example, by using the dyadic Green's functions to be discussed later. In the following we use ϵ_r for ϵ_{eff} and L and R for L' and R', respectively, with the difference understood.

Normal Modes and Feeder-Line Excitations. The normal modes excited in a microstrip patch antenna are usually transverse electric (*TE*) waves exhibiting no nodal points along the z axis, the direction perpendicular to the substrate plane. Thus, the normal mode solutions show no z dependence, and the electromagnetic components can be uniquely solved from E_z, satisfying the following Helmholtz equation

$$(\nabla_t^2 + k_{mn}^2)E_z = 0 \tag{7}$$

where ∇_t denotes the transverse part of the del operator (with respect to the z axis), k_{mn} is given by

$$k_{mn} = \omega_{mn}\sqrt{\mu_0\epsilon_0\epsilon_r} \tag{8}$$

ω_{mn} is the angular frequency, and $\{m, n\}$ refers to the index of the normal mode. The boundary condition imposed on E_z is that the derivative of E_z along the normal direction of the boundary vanishes at the magnetic wall. Once E_z is solved from Eq. (7), the corresponding $\boldsymbol{H}$ field is

$$\boldsymbol{H}_t = (j\omega\mu_0)^{-1}\boldsymbol{e}_z \times \nabla_t \boldsymbol{E}_z \tag{9}$$

where $\boldsymbol{e}_z$ denotes the unit vector along the z axis.

Let the rectangular patch be located at $0 \le x \le L$, and $0 \le y \le W$, [see Fig. 1]. The normal modes therefore are

$$E_z^{mn}(x, y) = \cos(m\pi x/L)\cos(n\pi y/W) \tag{10}$$

with the corresponding modal wavenumber

$$k_{mn} = [(m\pi/L)^2 + (n\pi/W)^2]^{1/2} \tag{11}$$

For a circular cavity of radius R the normal modes are, [see Fig. 2]

$$E_z^{mn}(\rho, \phi) = J_m(k_{mn}\rho)\exp(jm\phi) \tag{12}$$

and the modal wavenumber is determined by the zeroing condition of the derivative of Bessel functions of order m

$$J'_m(k_{mn}R) = 0 \tag{13}$$

and (ρ, ϕ, z) denotes the cylindrical coordinate.

Let us consider the patch antenna excited by either a microstrip line at the edge of the patch, Fig. 1. or a coax feeder directly under the patch, Fig. 2. The angular frequency of the external driving field is $\omega = 2\pi f$. We expect that cavity to be driven with maximum intensity when the frequency of excitation approaches the normal mode frequencies, Eq. (8). This phenomenon is generally known as forced oscillation, and it occurs commonly in many branches of physics. Thus, at resonance, the cavity is driven by the external field undergoing forced oscillation giving rise to maximum radiation efficiency. We first consider the excitation of the cavity by a microstrip feeder line. The boundary conditions for the cavity are that electric walls are located at metal boundaries and magnetic walls at the periphery which is not adjacent to the microstrip feeder line. At the input junction between the cavity and the feeder line, we define a window where we assume that the excitation currents are uniformly distributed, producing a uniform magnetic field there

$$\boldsymbol{H} = \boldsymbol{n} \times \boldsymbol{e}_z h_0 \tag{14}$$

Here $\boldsymbol{n}$ denotes the unit vector pointing outward along the normal direction of the window, and h_0 is a constant specifying the excitation current. In Fig. 1 the excitation-current window is located on the shad area directly under the microstrip feeder line with $\boldsymbol{n}$ being coincident with $-\boldsymbol{e}_y$. The excitation field governed by Eqs. (7) and (9) can be uniquely solved subject to the boundary condition of Eq. (14).

For the rectangular patch depicted in Fig. 1, let the microstrip feeder connection to the patch at the line segment $a \le x \le b$, and $y = 0$. The excitation field therefore is

$$E_z(x, y) = jk\zeta h_0 \sum_{m=0}^{\infty} A_m \cos\frac{m\pi x}{L} \cos\beta_m(W - y) \tag{15}$$

$$H_x(x, y) = h_0 \sum_{m=0}^{\infty} A_m \beta_m \cos\frac{m\pi x}{L} \sin\beta_m(W - y) \tag{16}$$

$$H_y(x, y) = -h_0 \sum_{m=0}^{\infty} A_m \frac{m\pi}{L} \sin\frac{m\pi x}{L} \cos\beta_m(W - y) \tag{17}$$

where

$$\beta_m = \sqrt{k^2 - \left(\frac{m\pi}{L}\right)^2} \tag{18}$$

$$\begin{aligned} k &= \omega\sqrt{\mu_0\epsilon_0\epsilon_r} \\ \zeta &= \sqrt{\frac{\mu_0}{\epsilon_0\epsilon_r}} \end{aligned} \tag{19}$$

$$A_m = \frac{4}{m\pi} \frac{\sin[m\pi(b-a)/2L]\cos[m\pi(b+a)/2L]}{\beta_m \sin \beta_m W} \qquad (m \neq 0) \tag{20}$$

and

$$A_0 = \frac{b-a}{Lk \sin kW} \tag{21}$$

Note that at $\omega = \omega_{mn}, A_m = \infty$, indicating that when the frequency of the external driving field equals one of the normal mode frequencies, only that normal mode will be excited in the cavity responsible for radiation. However, when losses are included, other modes with much smaller amplitudes can also be excited at resonance.

For the circular patch we consider the microstrip feeder line to join the metal patch at the arc $-\alpha \leq \phi \leq \alpha$, and $\rho = \boldsymbol{R}$. The excitation field can be then written as follows

$$E_z(\rho, \phi) = j\zeta h_0 \sum_{n=0}^{\infty} C_n J_n(k\rho)\cos(n\phi) \tag{22}$$

$$H_\rho(\rho, \phi) = \frac{h_0}{k\rho} \sum_{n=1}^{\infty} C_n n J_n(k\rho)\sin(n\phi) \tag{23}$$

$$H_\phi(\rho, \phi) = h_0 \sum_{n=0}^{\infty} C_n J_n'(k\rho)\cos(n\phi) \tag{24}$$

where

$$C_n = \frac{2\sin n\alpha}{n\pi J_n'(kR)} \qquad (n \neq 0) \tag{25}$$

$$C_0 = \frac{\alpha}{\pi J_0'(kR)} \tag{26}$$

and ζ and k are given in Eq. (19). Again, from Eqs. (25) and (26) it is seen that the coefficient of C_n goes to infinity if normal mode frequencies are approached [Eq. (13)].

Let us consider the excitation of the patch antenna by a coax line directly under the patch. We may assume the coax line to possess an inner filament of zero diameter ending in a point charge at the junction with the patch (see Fig. 2). The excitation current density therefore is

$$\boldsymbol{J}_e(x, y) = \boldsymbol{I}_0 \delta(x - x_0)\delta(y - y_0)\boldsymbol{e}_z, \text{ for a rectangular patch} \tag{27}$$

$$\boldsymbol{J}_e(\rho, \phi) = \boldsymbol{I}_0 \delta(\rho - \rho_0)\delta(\phi - \phi_0)/\rho \boldsymbol{e}_z, \text{ for a circular patch} \tag{28}$$

In the presence of a driving current it appears as an inhomogeneous term at the right-hand side of Eq. (7):

$$(\nabla_t^2 + k_{mn}^2)E_z = j\omega\mu_0 \boldsymbol{J}_e \cdot \boldsymbol{e}_z \tag{29}$$

The boundary conditions are the same as those leading to normal mode solutions—that is, electric walls at metal boundaries and magnetic walls at the periphery of the patch cavity. Thus, Eq. (29) can be solved in terms of normal mode solutions:

$$E_z(x, y) = \omega\mu_0 \sum_{m,n} \frac{E_z^{mn}(x, y)}{k^2 - k_{mn}^2} \frac{\displaystyle\int_0^L dx' \int_0^W dy' J_e(x', y') E_z^{mn}(x', y')^*}{\displaystyle\int_0^L dx' \int_0^W dy' |E_z^{mn}(x', y')|^2} \tag{30}$$

$$E_z(\rho, \phi) = j\omega\mu_0 \sum_{m,n} \frac{E_z^{mn}(\rho, \phi)}{k^2 - k_{mn}^2} \frac{\displaystyle\int_0^R d\rho' \int_0^{2\pi} \rho' d\phi' J_e(\rho', \phi') E_z^{mn}(\rho', \phi')^*}{\displaystyle\int_0^R d\rho' \int_0^{2\pi} \rho' d\phi' |E_z^{mn}(\rho', \phi')|^2} \tag{31}$$

Here Eqs. (30) and (31) are for a rectangular patch and a circular patch, respectively, and the normal modes, ${E_z}^{mn}{}_z(x, y)$ and ${E^{mn}}_z(\rho, \phi)$, are given in Eqs. (10) and (12). Equations (30) and (31) imply that when k approaches k_{mn}, the normal mode $\{m, n\}$ acquires an infinite amplitude. The corresponding magnetic field can be derived using Eq. (9).

Thus, for the rectangular patch, we have

$$E_z(x, y) = \frac{4j\omega\mu_0 I_0}{LW} \times \sum_{m,n=1}^{\infty} \frac{\cos(m\pi x_0/L)\cos(m\pi x/L)\cos(n\pi y_0/W)\cos(n\pi y/W)}{k^2 - k_{mn}^2} \tag{32}$$

$$H_x(x, y) = \frac{4I_0}{LW} \times \sum_{m,n=1}^{\infty} \frac{n\pi}{W} \frac{\cos(m\pi x_0/L)\cos(m\pi x/L)\cos(n\pi y_0/W)\sin(n\pi y/W)}{k^2 - k_{mn}^2} \tag{33}$$

$$H_y(x,y) = \frac{-4I_0}{LW} \times \sum_{m,n=1}^{\infty} \frac{m\pi}{L} \frac{\cos(m\pi x_0/L)\sin(m\pi x/L)\cos(n\pi y_0/W)\cos(n\pi y/W)}{k^2 - k_{mn}^2} \tag{34}$$

For the circular patch we have

$$E_z(\rho,\phi) = \frac{j\omega\mu_0 I_0}{\pi} \times \sum_{m=0}^{\infty}\sum_{n=1}^{\infty} \frac{(2-\delta_{m0})k_{mn}^2}{k^2 - k_{mn}^2} \frac{J_m(k_{mn}\rho)J_m(k_{mn}\rho_0)\cos[m(\phi-\phi_0)]}{(k_{mn}^2R^2 - m^2)[J_m(k_{mn}^2R^2)]^2} \tag{35}$$

$$H_\rho(\rho,\phi) = \frac{-I_0}{\pi\rho} \times \sum_{m=1}^{\infty}\sum_{n=1}^{\infty} \frac{m(2-\delta_{m0})k_{mn}^2}{k^2 - k_{mn}^2} \frac{J_m(k_{mn}\rho)J_m(k_{mn}\rho_0)\sin[m(\phi-\phi_0)]}{(k_{mn}^2R^2 - m^2)[J_m(k_{mn}^2R^2)]^2} \tag{36}$$

$$H_\phi(\rho,\phi) = \frac{I_0}{\pi} \times \sum_{m=0}^{\infty}\sum_{n=1}^{\infty} \frac{(2-\delta_{m0})k_{mn}^3}{k^2 - k_{mn}^2} \frac{J_m'(k_{mn}\rho)J_m(k_{mn}\rho_0)\cos[m(\phi-\phi_0)]}{(k_{mn}^2R^2 - m^2)[J_m(k_{mn}^2R^2)]^2} \tag{37}$$

where δ_{ij} is the Kronecker delta function and

$$\delta_{m0} = 1 \text{ if } m = 0 \text{ and } \delta_{m0} = 0 \text{ otherwise}$$

In Eqs. (32) to (34) and (35) to (37), k_{mn} is given by Eqs. (11) and (13), respectively, and ζ and k are defined in Eq. (19). Once the excitation fields are known, Eqs. (16) to (18), (22) to (24), (32) to (37), losses of various kinds, and hence the quality factor, Q, of the patch cavity can be calculated, as discussed later.

Input Impedance. Having solved the electromagnetic fields inside a lossless patch cavity, we can relax the assumption of perfect electric and magnetic walls and allow electromagnetic energy to propagate across these boundaries. This results in ohmic loss and radiation (surface wave) loss. Dielectric and magnetic losses occur in the interior of the patch cavity, assuming a lossy medium exhibiting complex permittivity and permeability, respectively. We consider first the radiation loss.

The Kirchhoff–Huygens principle, which is a vector analog of Green's theorem, states that the electromagnetic field inside a closed volume, V, can be derived by the volume charge and current distributions inside V and the surface charges and currents distributed on the enclosing surface of V, denoted as S. The effective

electric surface current density, $\boldsymbol{K}_{\mathrm{e}}$, magnetic surface current density, $\boldsymbol{K}_{\mathrm{m}}$, and electric surface charge density, Σ, are (7), respectively,

$$\boldsymbol{K}_{\mathrm{e}} = -\boldsymbol{n} \times \boldsymbol{H} \qquad \boldsymbol{K}_{\mathrm{m}} = \boldsymbol{n} \times \boldsymbol{E} \qquad \Sigma = -\epsilon \boldsymbol{n} \cdot \boldsymbol{E} \tag{38}$$

where $\boldsymbol{n}$ denotes the unit outward vector normal to S, and ϵ is the permittivity. Thus, if we consider the outside volume of the patch cavity as the volume V, we conclude that the effective magnetic current density on the magnetic wall is

$$\boldsymbol{K}_{\mathrm{m}} = -2\, \boldsymbol{n} \times \boldsymbol{e}_z E_z \tag{39}$$

where $\boldsymbol{n}$ denotes the unit outward vector normal to the magnetic wall, with sign opposite that is Eq. (38), and the factor of two accounts for the presence of the ground plane. $\boldsymbol{K}_{\mathrm{e}}$ and Σ do not appear on a magnetic wall.

The radiation field arising from the magnetic current density $\boldsymbol{K}_{\mathrm{m}}$ can be derived by using the same formula describing the electric current density $\boldsymbol{K}_{\mathrm{e}}$ converted from the duality rule (7). The duality rule states that the electromagnetic theory remains valid if all of the elic quantities are changed into the corresponding magnetic quantities and the magnetic quantities are changed into the negative of the corresponding electric quantities. Thus, the vector potential associated with $\boldsymbol{K}_{\mathrm{m}}$ can be written as (8)

$$\begin{aligned} \boldsymbol{A}_m(\boldsymbol{r}) &= \frac{\epsilon_0 d}{4\pi} \oint_{C_{\mathrm{m}}} dl' \frac{\boldsymbol{K}_{\mathrm{m}}(\boldsymbol{r}')}{|\boldsymbol{r} - \boldsymbol{r}'|} e^{-jk_0|r-r'|} \\ &\approx \frac{\epsilon_0 d}{4\pi} \frac{\exp(-jk_0 r)}{r} \oint_{C_{\mathrm{m}}} dl' \boldsymbol{t}' E_z(\boldsymbol{r}') \exp(jk_0 \boldsymbol{e}_r \cdot \boldsymbol{r}') \end{aligned} \tag{40}$$

where d denotes the thickness of the substrate, C_{m} the contour of the magnetic wall with counterclockwise tangential unit vector $\boldsymbol{t}$, $\boldsymbol{e}_{\mathrm{r}}$ the unit vector along $\boldsymbol{r}$, a vector connecting the coordinate origin toward the observation point, and

$$k_0 = \omega(\mu_0 \epsilon_0)^{1/2} \tag{41}$$

is the wavenumber in air. In Eq. (40) primed quantities originate at the source and assume $|\boldsymbol{r} - \boldsymbol{r}'| \gg d$.

The fields in the far-zone are

$$\boldsymbol{H}(\boldsymbol{r}) = -j\omega \boldsymbol{A}_{\mathrm{m}}(\boldsymbol{r}) \tag{42}$$

$$\boldsymbol{E}(\boldsymbol{r}) = -\zeta_0 \boldsymbol{e}_r \times \boldsymbol{H}(\boldsymbol{r}) \tag{43}$$

where

$$\zeta_0 = (\mu_0/\epsilon_0)^{1/2} \tag{44}$$

is the wave impedance in air (= 377 Ω). We therefore have

$$\mathbf{E}(\mathbf{r}) \approx \frac{j\varepsilon_0 k_0 d}{4\pi}\frac{\exp(-jk_0 r)}{r} \oint_{C_m} dl'(-\boldsymbol{t}'\cdot\boldsymbol{e}_\phi\boldsymbol{e}_\theta + \boldsymbol{t}'\cdot\boldsymbol{e}_\theta\boldsymbol{e}_\phi)E_z(\boldsymbol{r}')\exp(jk_0\boldsymbol{e}_r\cdot\boldsymbol{r}'), \quad (45)$$

where $\boldsymbol{e}_\theta$ and $\boldsymbol{e}_\phi$ denote unit vectors along the θ and ϕ directions at the observation point $\boldsymbol{r}$. By using Eq. (45) the far-field radiation associated with a circular patch antenna fed by a microstrip line, Eq. (22), is, for example,

$$\boldsymbol{E}(\boldsymbol{r}) \approx \frac{\alpha\zeta h_0 k_0 d}{\pi}\frac{R\exp(-jk_0 r)}{r} \times \sum_{m=-\infty}^{\infty} j^{-m}\frac{J_m(kR)}{J'_m(kR)}\frac{\sin m\alpha}{m\alpha}e^{-jm\phi} \cdot\left[\boldsymbol{e}_\theta J'_m(k_0 R\sin\theta) + j\boldsymbol{e}\theta\cos\theta\frac{mJ_m(k_0 R\sin\theta}{k_0\sin\theta}\right], \quad (46)$$

where it is understood that the ratio of sin $m\alpha$ to $m\alpha$ is 1 when $m = 0$. The far-field radiation pattern can be calculated by using the following equation:

$$\frac{dP_r}{d\Omega} = \lim_{r\to\infty}\frac{r^2|E|^2}{2\zeta_0} \quad (47)$$

and the total radiated power is then

$$P_r = \int_o^\pi \sin\theta\, d\theta \int_o^{2\pi} d\phi\,\frac{dP_r}{d\Omega} \quad (48)$$

Conductor loss and dielectric loss can be derived with ease (7). The conductor loss is given by

$$P_c = R_s \iint_{S_c} |\boldsymbol{H}|^2\, ds \quad (49)$$

where S_c denotes the metal surface with R_s the surface resistance

$$R_s = \sqrt{\frac{\omega\mu_0}{2\sigma}} \quad (50)$$

and σ is the conductivity of metal. The dielectric loss is given by

$$P_d = \frac{\omega\epsilon_r\epsilon_0\,\tan\delta}{2}\iiint_{V_c}|E_z|^2\, dv \quad (51)$$

where V_c denotes the volume of the cavity and tan δ is the dielectric loss tangent.

The radiation or antenna efficiency is the ratio of radiated power to input power, or

$$e = \frac{P_r}{P_r + P_c + P_d} \times 100\% \tag{52}$$

The total stored electric energy is then

$$W_e = \frac{\epsilon_r \epsilon_0}{4} \iiint_{V_c} |E_z|^2 \, dv = \frac{P_d}{2\omega \tan\delta} \tag{53}$$

Since, by definition, at resonance the stored magnetic energy, W_m, equals the stored electric energy, W_e, we have for the total stored electromagnetic energy

$$W_T = W_e + W_m = \frac{P_d}{\omega \tan\delta} \tag{54}$$

From the definition of Eq. (1), the total Q factor of the cavity is

$$Q = \frac{W_T}{P_r + P_c + P_d} \tag{55}$$

upon which the voltage standing wave ratio (*VSWR*) bandwidth can be defined. We define S_{max} to be the maximum value of VSWR that can be tolerated. We then have (9)

$$\text{VSWR bandwidth}\,(\%) = \frac{100(S_{max} - 1)}{Q\sqrt{S_{max}}} \tag{56}$$

Typically, $S_{max} = 2$.

The input susceptance B, of the antenna can be calculated from the lossless patch cavity, which is a zeroth-order quantity. However, the input conductance, G, must be calculated from the total loss of the cavity, which is a first-order quantity. Thus

$$jB = -I/V \tag{57}$$

$$G = (P_r + P_c + P_d)/|V|^2 \tag{58}$$

where I and V are the averaged input current and voltage experienced at the input feeder position. For a coax feed with excitation current expressed by Eqs. (27) and (28), assuming a thin inner filament as shown in Fig. 2, I is known and V can be calculated from E_z evaluated at the input position multiplied by the thickness of the substrate d. We therefore have

$$B^{-1} = \frac{4d\omega\mu_o}{LW} \sum_{m,n=1}^{\infty} \frac{\cos^2(m\pi x_o/L)\cos^2(n\pi y_o/W)}{k^2 - k_{mn}^2} \tag{59}$$

$$B^{-1} = \frac{d\omega\mu_o}{\pi} \sum_{m=0}^{\infty} \sum_{n=1}^{\infty} \frac{(2-\delta_{m0})k_{mn}^2}{k^2 - k_{mn}^2} \frac{[J_m(k_{mn}\rho_o)]^2}{(k_{mn}^2 R^2 - m^2)[J_m(k_{mn}^2 R^2)]^2} \tag{60}$$

for rectangular and circular patch antennas, respectively. For a microstrip feed, the input voltage is obtained according to Faraday's law by averaging E_z over the feeder-line window joining the cavity multiplied by the thickness of the substrate, d. The input current can be derived by applying Ampere's law at the feeder-line window, which is h_o times the transverse length of the window, that is, $h_o\,(b-a)$ for the rectangular antenna and $h_o\,(2\alpha R)$ for the circular antenna. We therefore have

$$B^{-1} = \frac{\zeta d}{L}\left[\operatorname{ctn} k\mathrm{W} + \sum_{m=1}^{\infty} \frac{8}{(m\pi)^2} \frac{L^2}{(b-a)^2} \frac{k}{\beta_m} \operatorname{ctn}\beta_m \mathrm{W} \left(\sin\frac{m\pi(b-a)}{2L} \cos\frac{m\pi(b+a)}{2L}\right)^2\right] \tag{61}$$

$$B^{-1} = \frac{\zeta d}{2\pi R}\left(\frac{J_0(kR)}{J_0'(kR)} + \sum_{n=1}^{\infty} \frac{2\sin^2 n\alpha}{n^2\alpha^2} \frac{J_n(kR)}{J_n'(kR)}\right) \tag{62}$$

for rectangular and circular patch antennas, respectively. Here k_{mn} in Eq. (60) is given by Eq. (13) and β_{m} in Eq. (61) is given by Eq. (18).

From Eqs. (59), (60) and (62), we note that at the normal mode frequencies the input susceptance $B = 0$, and hence $B^1 = \infty$. These points are called antiresonance points as plotted in the Smith chart (see Fig. 3, example for). The resonant points are defined to be purely resistive when the input resistance of the antenna matches the feeder-line impedance, resulting in zero reflection. Therefore, $B^{-1} = 0$ at resonance. The resonance point occurs slightly above the antiresonance frequency, which requires participation of normal modes of all orders, although the normal mode responsible for antiresonance is excited with the greatest intensity. Thus, by definition, at resonance the capacitive part of the stored energy equals the inductive part, rendering the overall input reactance zero. In calculating the susceptance, we should also include the capacitance associated with near-field excitation. However, its contribution has been accounted for as the increment in the effective resonance length of the antenna, [See Eqs. (2) and (5)]. The input impedance is

$$Z = (G + jB)^{-1} \tag{63}$$

We note that, in reality, at antiresonance, B is finite due to the presence of losses occurring at the antenna patch cavity.

One severe drawback of the cavity model is that it is not able to address the surface-wave loss. 10 estimated that surface-wave excitation is not important if $d/\lambda_0 < 0.09$ for $\epsilon_r = 2.3$ and $d/\lambda_0 < 0.03$ for $\epsilon_r = 10$, where λ_0 is the free-space wavelength. The criterion given by 11 is more quantitative: $d/\lambda_0 < 0.07$ for $\epsilon_r = 2.3$, and $d/\lambda_0 < \quad 0.0023$ for $\epsilon_r = 10$, if the antenna is to emit no more than 25 percent of the total radiated power as surface waves. Recent work by Fonseca et al. showed that the size of the patch is also a parameter (12), as discussed in more detail in the next section. When ferrite material is used as the substrate, magnetic loss can be estimated

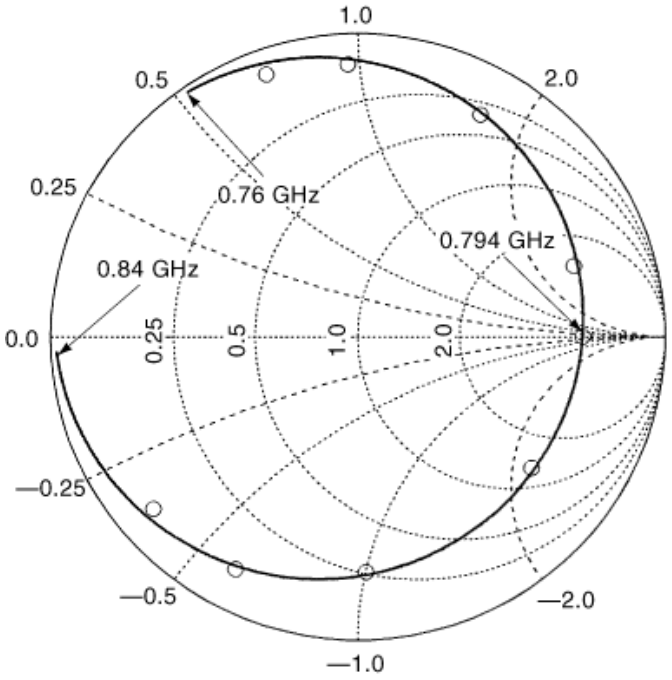

Fig. 3. Integration contours for Sommerfeld integrals illustrating contribution from spatial wave and surface wave excitations.

using a formula similar to Eq. (51):

$$P_m = \frac{\omega \mu''}{2} \iiint_{V_c} |\boldsymbol{H}|^2 \, dv \tag{64}$$

where μ'' denotes the imaginary part of the permeability. In concluding this section we note that the cavity model depicts a semiempirical picture where the parameters have been adjusted to fit experiments, for example, the effective dielectric constant ϵ_{eff}, Eq. (3), and the increment in the resonant length of the patch, Δ, Eqs. (2) and (5). Nevertheless, the calculated radiation pattern and input impedance compare very well with measurements (13).

Dyadic Green's Function

As we have mentioned in the previous section, the open structure of a microstrip patch antenna can be rigorously accounted for only in a full-wave analysis resorting to numerical solutions. Maxwell's equations can be explicitly solved numerically in the frequency domain or in the time domain using the generic 3-D finite-element and finite-difference methods (14). However, it is more informative to use the dyadic Green's functions, since the electromagnetic fields generated by a point dipole-current source has already been solved analytically in the same microstrip geometry, which is termed the dyadic Green's function. The electromagnetic fields excited by a patch antenna can then be composed as superposition's of the point-dipole solutions in the

context of a conventional Green's function method. The numerical technique applies only when the Galerkin method is used to solve the resultant integral equations relating the unknown current variables to local electric fields distributed across the metal patch boundaries.

The physical meaning of the Green's function is clear, and surface waves have been used with equal importance as spatial waves in the Green's function formalism. Furthermore, the Green's function solution usually requires 2-D calculations, in contrast to the generic 3-D computational methods. This is true when the metal thickness is much smaller than the thickness of the substrate, as is usually the case. Material losses can be readily included in the Green's function if complex permittivity and permeability values are used. It turns out that efficient CAD tools can be constructed using the dyadic Green's function solutions, which calculate engineering parameters of a microstrip antenna, including radiation frequency, far-field pattern, efficiency, input impedance, and so on and analyze the cross-talk problem inherent in common microstrip circuitries.

To illustrate the physics in the application of a Green's function, we have decided not to regenerate many mathematical formulas in this section. Instead, we concentrate on Sommerfeld's approach to the Green's function analysis (1), because it lends itself to a more physical understanding of the problem. We wish to introduce the methodology leading to the formulation of the dyadic Green's function for a general stratified structure, consisting of a finite number of dielectric and magnetic layers as constituents. We assume this layered structure is infinite in both horizontal and vertical directions, although it is possible to include finite substrate and radiation space by employing periodic boundary conditions, for example. Also, we assume the current distribution is two-dimensional, resulting in 2-D analysis on the Galerkin elements. The finite conductivity of the ground plane can be accounted for by invoking complex permittivity of the conductor layer (1). Results of calculations are cited mainly from Ref. 15. Background material can be found in Ref. 16.

Point-Dipole Solutions. We start by introducing the vector potential, $\boldsymbol{A}$, and scalar potential, V, in electrodynamics subject to a Lorentz gauge (17), which has been implicitly used by 1

$$\boldsymbol{H} = (1/\mu_0)\nabla \times \boldsymbol{A} \tag{65}$$

$$\boldsymbol{E} = -j\omega\boldsymbol{A} - \nabla V \tag{66}$$

$$\nabla \cdot \boldsymbol{A} + j\omega\mu_0\epsilon V = 0 \tag{67}$$

This results in uncoupled equations for $\boldsymbol{A}$ and V as follows:

$$(\nabla^2 + k^2)\boldsymbol{A} = -\mu_0\boldsymbol{J} \tag{68}$$

$$(\nabla^2 + k^2)V = (-1/\epsilon_0)\rho \tag{69}$$

where $\boldsymbol{J}$ and ρ are the current and charge densities, respectively, and normally $\rho = 0$ (oscillating charges can not easily be realized physically). We note that Eq. (68) does not specify $\boldsymbol{A}$ uniquely for a finite volume under consideration (17). However, this gauge freedom is almost fixed for a system of infinite volume, because the only source-free radiation for the entire space are the incoming waves from infinity, which can be readily checked out and excluded from the solution of $\boldsymbol{A}$ by performing proper gauge transformation. From Eq. (67), the scalar potential V is obtained from the divergence of $\boldsymbol{A}$, and hence only the vector potential $\boldsymbol{A}$ needs to be solved.

We are now solving the vector potential, $\boldsymbol{A}(x, y, z)$, Eq. (68), induced by a point dipole current source, $\boldsymbol{J}_0(x, y, z)$, in the background of a dielectric or magnetic layered structure. A point dipole is also called a Hertzian

dipole, which can be approximated by a dipole antenna whose arms are much smaller than the wavelength of radiation (1). Assuming the point dipole to be located at (0, 0, z_0), the current density associated with the point dipole is

$$\boldsymbol{J}_0(x, y, z) = \boldsymbol{I}_0 d\ell\, \delta(x)\delta(y)\delta(z - z_0) \tag{70}$$

where $\boldsymbol{I}_0\, dl$ (= finite) denotes the strength of the dipole. Without loss of generality we assume $\boldsymbol{I}_0$ is along the x direction. From Eq. (68) we know that A_x is nonzero, corresponding to the radiation field from a horizontal dipole. This is the only field that would be induced in empty space by the point dipole of Eq. (70). In the presence of the layered structure, however, A_z is also nonzero, because of the oblique reflection of A_x from the layer interfaces, corresponding to the radiation field from a vertical dipole in the absence of the stratified structure. Finally, A_y is identically zero as implied by the symmetry of the problem.

We require the tangential components of $\boldsymbol{E}$ and $\boldsymbol{H}$ to be continuous across the layer interfaces, which can be directly written down from Eqs. (65) and (66). According to 1, these boundary conditions can be integrated with respect to the transverse coordinates, x and y, and the constants of integration can be justified as zeros by letting x and y go to infinity. For example, suppose one boundary condition requires the derivative of the function $f(x, y, z)$ with respect to x to be continuous across an interface. If $f(x, y, z)$ vanishes as x goes to infinity, either decreasing exponentially to zero as for a decaying wave or averaging to zero as for an oscillating wave, we can integrate this boundary condition with respect to x and conclude that the function $f(x, y, z)$ itself must be continuous across the interface. As such, the boundary conditions imposed on the vector potential $\boldsymbol{A} = A_x\, \boldsymbol{e}_x + A_z\, \boldsymbol{e}_z$ as derived by Sommerfeld are the continuity conditions on the following four quantities (1)

$$\epsilon\mu A_x,\ \epsilon\mu(\partial A_x/\partial z), \epsilon\mu A_z,\ \text{and}\ \partial A_x/\partial x + \partial A_z/\partial z \tag{71}$$

Therefore there are four boundary conditions at each layer interface.

Recognizing the fact that the layered structure is homogeneous in the transverse directions, say, x and y, it implies that the Helmholtz equation, Eq. (68), can be conveniently solved in the transverse Fourier-spectral domain. For a given transverse spectral vector, $\boldsymbol{k}_t = [k_x, k_y]$, we denote the corresponding spectral-domain vector potential components as $\tilde{A}_x(k_x, k_y, z)$ and $\tilde{A}_x(k_x, k_y, z)$ which relate to $A_x(x, y, z)$ and $A_x(x, y, z)$ via double Fourier integrals, respectively. For each layer that does not contain the dipole source, we solve the Helmholtz equation, Eq. (68), to obtain the following solutions:

$$\tilde{A}_x(k_x, k_y, z) = a\, \exp(+\gamma z) + b\, \exp(-\gamma z) \tag{72}$$

$$\tilde{A}_z(k_x, k_y, z) = c\, \exp(+\gamma z) + d\, \exp(-\gamma z) \tag{73}$$

where a, b, c, d are four unknowns to be determined by the boundary conditions and γ is given by

$$\gamma^2 = k_x^2 + k_y^2 - \epsilon\mu\omega^2 \tag{74}$$

where ϵ and μ are the permittivity and permeability of the layer under consideration. For the uppermost layer $a = 0 = c$ and for the lower most layer $b = 0 = d$, as required by the boundary conditions at $z = \pm\infty$. For the layer that contains the dipole source, we integrate Eq. (68) from $z = z_0{}^- \ z = z_0{}^+$ and note that the double Fourier transform of the function $\delta(x)\ \delta(y)$ is $1/2\pi$, and we derive the following discontinuity requirement on

$\partial \bar{A}_{z_x}(k_x, k_y, z)/\partial z$ on both sides of the plane $z = z_0$

$$\partial \tilde{A}_x(k_x, k_y, z^+)/\partial z - \partial \tilde{A}_x(k_x, k_y, z^-)/\partial z = -I_0 d\ell/2\pi \qquad (75)$$

We therefore insert a fictitious interface at $z = z_0$ assuming different values of *a, b, c, d* of for the two subregions above and below this interface [Eqs. (72) and (73)], but with the same value of γ [Eq. (74)]. The boundary conditions imposed on this fictitious interface are the same as before, except that the requirement on the continuity of the quantity $\epsilon\mu(\partial A_x/\partial z)$ is now being replaced by Eq. (75). If the z_0 plane occurs at a single layer interface of the stratified structure, no virtual interface needs to be created; we need only replace the continuity requirement on $\mu(\partial A_x/\partial z)$ by Eq. (75).

Thus, we arrive at $4N$ unknowns with $4N$ boundary conditions for N interfaces, including the fictitious one, if there is one. In the boundary conditions we replace [Eq. (71)] the operator $\partial/\partial x$ by $-jk_x$, and $\partial/\partial z$ by $\pm\gamma$, whichever is applicable according to Eqs. (72) and (73). The $4N$ boundary conditions now become algebraic ones and hence the $4N$ unknowns can be solved. The amplitudes of these unknowns are all proportional to the dipole strength I_0 d l, which can be conveniently chosen to be 1, as required by the Green's function. The vector potentials $A_x(x, y, z)$ and $A_z(x, y, z)$ can then be solved from $\bar{A}_{z_x}(k_x, k_y, z)$ and $\bar{A}_{z_x}(k_x, k_y, z)$ by applying the inverse two-dimensional Fourier transforms. The electric and magnetic fields can finally be obtained by using Eqs. (65) to (67).

Material imperfection results in losses of various kinds, upon which the permittivity and permeability values become complex numbers. The dielectric loss is described by a loss tangent, tanδ, and the permittivity takes the form of $\epsilon_0\epsilon_r(1 - j\tan\delta)$, where ϵ_r denotes the dielectric constant. For a demagnetized magnetic substrate, the permeability is $\mu_0(\mu' + j\mu'')$ and μ' and μ'' are the real and imaginary parts of the relative permeability (3). For a metal conductor the permittivity contains both the displacement current and the conduction current and hence the permittivity is modified as $\epsilon_0 - j\sigma/\epsilon$, where σ denotes the conductivity. This is the permittivity that was explicitly considered by 1, solving the electromagnetic fields generated by a Hertzian dipole in response to the earth's surface.

If a perfect metal is used as the ground plane, the electromagnetic field will not penetrate into it. Therefore, the boundary condition on the metal surface is that the tangential components of the electric field vanish, and it implies

$$\boldsymbol{A}_x = 0, \text{ and } \partial A_x/\partial x + \partial A_z/\partial z = 0 \qquad (76)$$

Thus, we have $4N - 2$ unknowns and $4N - 2$ boundary conditions for a layered structure possessing a perfect metal ground plane.

Actually, the interface boundary conditions [Eq. (71)] specify the flection and transmission of electromagnetic waves from one layer to another, and $\bar{A}_{z_x}$ is proportional to the magnetic field component and $\bar{A}_{z_z}$ is proportional to the electric field component. Oblique-angle reflection and transmission can be readily written down in terms of Snell's law (18) and hence the coefficients of $\bar{A}_{z_x}$ and $\bar{A}_{z_z}$, [Eqs. (72) and (73)] are determined with relation to the preceding and succeeding layers. Thus, without the need of solving the boundary conditions explicitly, [Eq. (71)], all of the *a, b, c, d* coefficients for the layers are correlated with each other and only four unknowns remain, corresponding to those at the outermost layers (top and bottom), which can now be solved by using the boundary conditions at the fictitious interface imposed by the point dipole [Eq. (75)], and so on. For example, if the last layer is a perfect metal, the *a, b, c, d* coefficients of the layer adjacent to it satisfy the following relationships

$$b = -a \qquad d = c \qquad (77)$$

which are recognized as the total reflection condition. Equation (77) can be shown to be identical to Eq. (76).

For completeness, we list the transverse spectral-domain vector potential induced by a horizontal point dipole located on top of a dielectric substrate backed by a perfect metal ground plane

$$\begin{aligned}\tilde{\mathrm{A}}_x(k_x, k_y, z) &= (\mu_0/2\pi)\exp(-\gamma_0 z)/D_{\mathrm{TE}} \\ \tilde{\mathrm{A}}_z(k_x, k_y, z) &= (\mu_0/2\pi)(\epsilon_r - 1)jk_x \exp(-\gamma_0 z)/(D_{\mathrm{TE}} D_{\mathrm{TM}}), \\ &\quad \text{for } z > 0\end{aligned} \tag{78}$$

$$\begin{aligned}\tilde{\mathrm{A}}_x(k_x, k_y, z) &= (\mu_0/2\pi)\sinh\gamma(z+d)/(D_{\mathrm{TE}}\sinh\gamma d) \\ \tilde{\mathrm{A}}_z(k_x, k_y, z) &= (\mu_0/2\pi) \\ &\quad (\epsilon_r - 1)jk_x \cosh\gamma(z+d)/(D_{\mathrm{TE}} D_{\mathrm{TM}}\cosh\gamma d), \\ &\quad \text{for } 0 > z > -h\end{aligned} \tag{79}$$

and D_{TE} and D_{TM} are defined by

$$D_{\mathrm{TE}} = \gamma_0 + \gamma \coth \gamma d, \tag{80}$$

$$D_{\mathrm{TM}} = \epsilon_r \gamma_0 + \gamma \tanh \gamma d, \tag{81}$$

Here the dipole is located at the plane $z = 0$, the dielectric substrate is of a thickness d and permittivity ϵ, and γ_0 and γ are given by Eq. (74) with subscript 0 referring to air. The zeros of Eqs. (80) and (81) correspond to surface-wave TE and TM modes, respectively. While there exists at least one TM surface mode, it is not always the case that TE surface modes will be excited. The threshold for TE mode excitation is

$$k_0 d(\epsilon r - 1)^{1/2} < \tau/2$$

$$f[GHz] < 75/\{d[\mathrm{mm}](\epsilon_r - 1)^{1/2}\} \tag{82}$$

Sommerfeld Integrals. Within each layer the dipole field solutions are obtained by inverse Fourier transforms of $\tilde{A}_{x\mathrm{x}}(k_x, k_y, z)$ and $\tilde{A}_{xz}(k_x, k_y, z)$ over the two-dimensional $k_x - k_y$ plane, or, equivalently, $k_\rho - k_\phi$ plane. Here (k_ρ, k_ϕ) denotes the polar coordinate and (k_x, k_y) the Cartesian coordinate. In general

$$\tilde{A}_x(k_x, k_y, z) = f(k_\rho, z) \tag{83}$$

and

$$\tilde{A}_x(k_x, k_y, z) = k_x g(k_\rho, z) = \cos k_\phi k\rho g(k_\rho, z) \tag{84}$$

as can be checked from the boundary condition of Eq. (71). In other words, $\tilde{A}_{xx}$ is an even function of k_x and $\tilde{A}_{xz}$ is an odd function of k_x, as implied by the symmetry of the problem. Therefore, after integration over k_ϕ, we

obtain

$$A_x(\rho, \phi, z) = \int_0^\infty J_o(k_\rho \rho) k_\rho f(k_\rho, z) dk_\rho \qquad (85)$$

$$A_z(\rho, \phi, z) = j \cos\phi \int_0^\infty J_1(k_\rho \rho) k_\rho^2 g(k_\rho, z)\, dk_\rho \qquad (86)$$

Although, Eqs. (85) and (86) can be numerically integrated, as discussed later, it is instructive to discuss a procedure outlined by 1. Actually, Eqs. (85) and (86) are termed Sommerfeld integrals. The most significant discovery of Sommerfeld was that the seemingly real integration starting at the fixed point $k_\rho = 0$ can be converted into a complex k_ρ integration over a path, W, that closes at infinity (See Fig. 4

$$A_x(\rho, \phi, z) = \frac{1}{2} \int_W h_0^2(k_\rho \rho) k_\rho f(k_{\rho,z})\, dk_\rho \qquad (87)$$

$$A_z(\rho, \phi, z) = \frac{j \cos\phi}{2} \int_W H_1^{(2)}(k_\rho \rho) k_\rho^2 g(k_\rho, z)\, dk_\rho \qquad (88)$$

where $H_0{}^{(2)}$ are Hankel functions of the second kind of order 0 and 1, respectively. In Fig. 4, the contour W is detoured slightly in the complex k_ρ plane in order not to run into branch cuts and poles such that the integrands remain finite and single valued. Only two-layer substances are illustrated in Fig. 4, where the air is denoted by the subscript 0 and a dielectric layer is denoted by the subscript 1. For example, the respective permittivities for air and the dielectric layer are ϵ_0 and ϵ_1 (the permeability of the dielectric layer is assumed to be μ_0, the same as air). In Fig. 4, k_0 and k_1 are the branch points given by

$$k_0 = (\epsilon_0 \mu_0)^{1/2} \qquad k_1 = (\epsilon_1 \mu_0)^{1/2} \qquad (89)$$

and ρ is the smallest zero assumed by the function D_{TM}, see Eq. (81). It is understood that more branch points, and hence more branch cuts, will appear in Fig. 4 if more layers are presented in the layered structure. Also, more simple poles will appear if D_{TE} and D_{TM} of Eqs. (80) and (81) admit more zeros. In Fig. 4, the branch point at $k_\rho = 0$ is associated with the Hankel functions $H_0{}^{(2)}$; For Eq. (88), this branch point, and hence its associated branch cut, is replaced by a simple pole due to the different singular behavior of $H_1{}^{(2)}$ at the origin.

According to Sommerfield, the couour W shown in Fig. 4 can be analytically deformed into three or more components surrounding the respective branch cuts and simple pole, denoted as Q_0, Q_1, and P. 1 showed that contour integrals of Q_0 and Q_1 give rise to spatial wave radiation, and for a large (spherical) distance r, they exhibit the following asymptotic dependence

$$Q_0(Q_1) \propto \exp(-jk_0 r)/r \qquad (90)$$

Actually, Q_0 is due to the free-space dipole radiation, and Q_1 is the radiation wave diffracted by the dielectric layer (or from the image dipole induced by that layer) (1). Assume the air-dielectric interface is

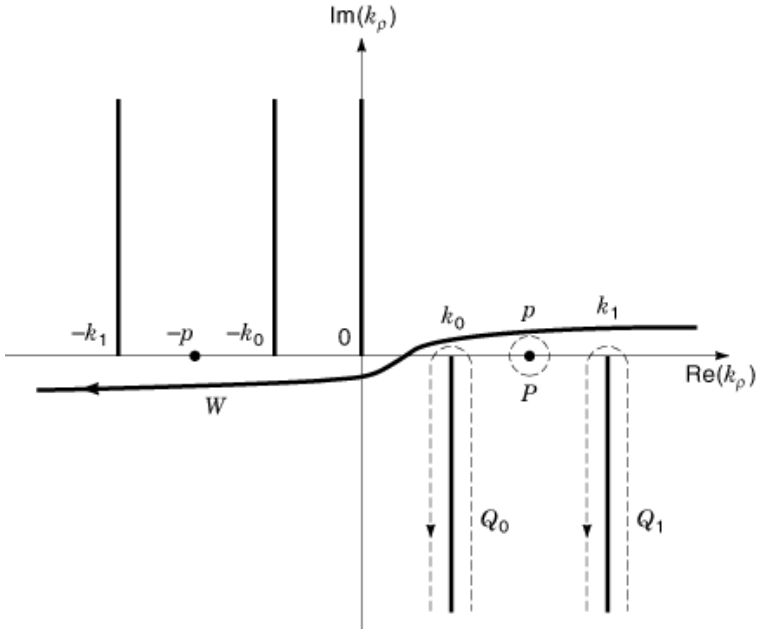

Fig. 4. Input impedance loci of the cited antenna. The solid line is from calculation, and small circles represent measurements made in Ref. 13.

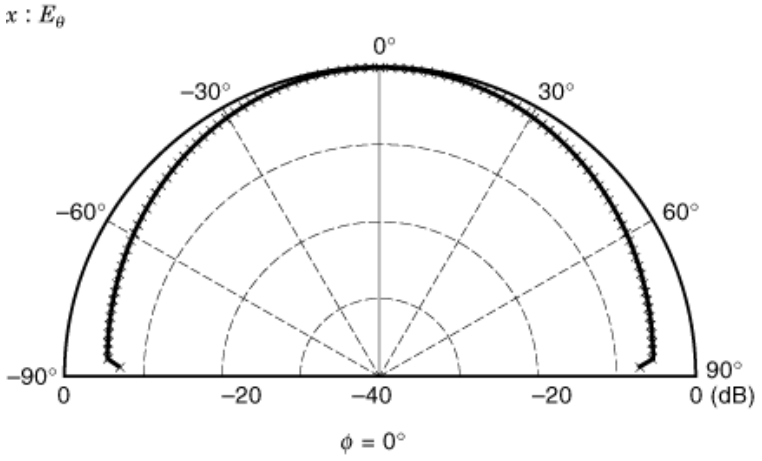

Fig. 5. Radiation profile of the cited antenna (13) in the $\phi = 0^\circ$ plane.

located at $z = 0$. For $z > 0$, contribution form contour P has the following asymptotic forms

$$P \propto H_0^{(2)}(p\rho)\exp[-\sqrt{p^2 - k_0^2}z], \text{ for } A_x \text{ [see Eq. (86)]} \quad (91)$$

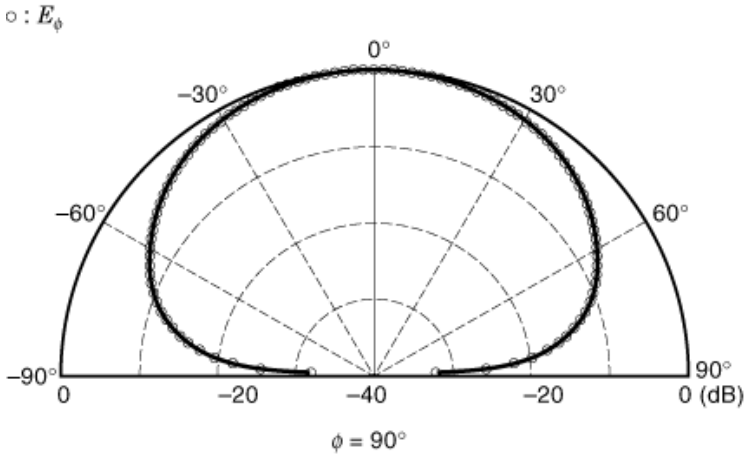

Fig. 6. Radiation profile of the cited antenna (13) in the $\phi = 90^\circ$ plane.

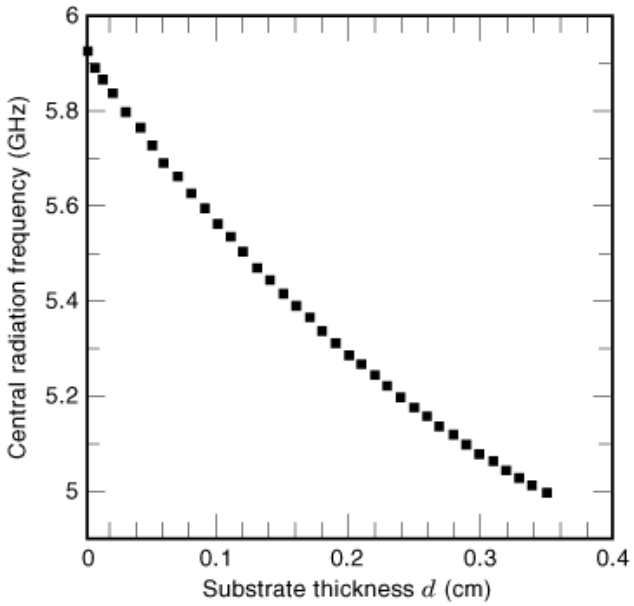

Fig. 7. Calculated radiation frequency as a function of substrate thickness (fed by microstrip line).

$$P \propto \cos\phi H_1^{(2)}(p\rho)\exp[-\sqrt{p^2 - k_0^2}z], \text{ for } A_z[\text{see Eq. (87)}] \quad (92)$$

They are surface waves tied to the interface and decrease at a rate proportional to $1/\sqrt{\rho}$ in the lateral directions, in contrast to the spatial wave radiation exhibiting a $1/r$ dependence, [Eq. (90)].

In the presence of material losses, the branch points and simple poles associated with spatial and surface waves, respectively, acquire imaginary components, which are then pushed off from the real axis toward the lower half of the complex k_ρ plane. As such, numerical integration of Eqs. (65) and (66) can be properly carried

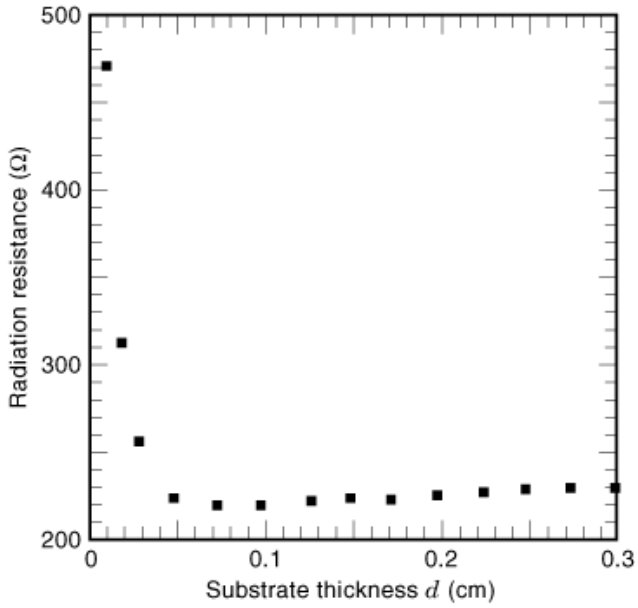

Fig. 8. Calculated radiation resistance as a function of substrate thickness (fed by microstrip line).

out. However, care needs to be taken to avoid large truncation errors. Integration of k_ρ along the real positive axis can be distinguished in three regions

Region I $0 < k_\rho < k_0$
Region II $k_0 < k_\rho < k_c$
Region III $k_c < k_\rho < \infty$

Here, k_c denotes a cutoff wavenumber to be discussed later. In Region I the integrands are well behaved. However, at the resonant frequencies of a metal patch dictated by the cavity model, both the numerator and denominator of the integrand vanish, although their ratio remains finite. We call these geometric resonant points quasisingularities (15). Near these quasisingular points the numerator and denominator need to be expanded in Taylor series upon which their common zeros cancel out.

All of the surface poles are contained in Region II, and, conventionally, the upper bound of Region II, k_c, is defined to be 10 times the real part of the largest surface pole occurring at the integrand. In Region II the integrand behaves wildly in the vicinity of a surface pole. When coming across a surface pole, the integrand transits from positive infinity to negative infinity, resulting in sharp cancellation during numerical integration. To circumvent this difficulty we expand the integrand in Laurent series in the vicinity of a surface pole $k_p = p$, and the quasisingular terms (with negative exponents) are then evaluated analytically (remember p is now a complex number). Equivalently, the singular part of integration is obtained via residual calculations. After the singular part is subtracted from the integrand, the integrand becomes regular and can then be numerically integrated in Region II.

In Region III we are involved with integration of Bessel functions at infinity, which oscillate indefinitely as infinity is approached without exhibiting a strict period. This renders the conventional extrapolation scheme

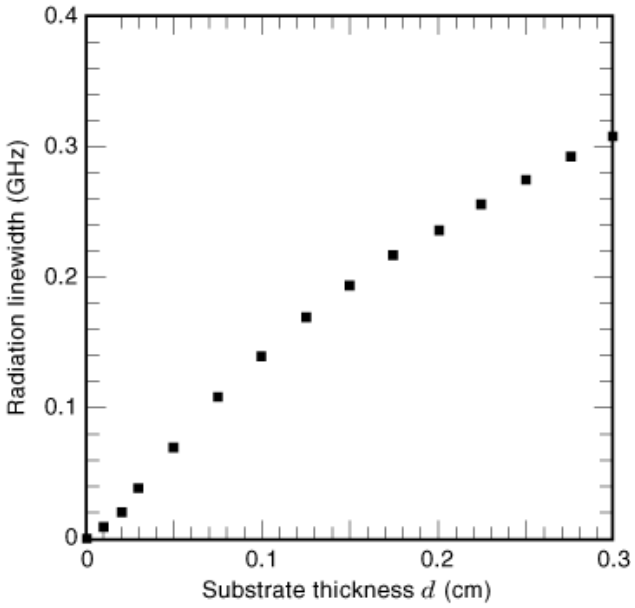

Fig. 9. Calculated radiation linewidth as a function of substrate thickness (fed by microstrip line).

inaccurate. To perform integration in this region we consider asymptotic expansion of Bessel functions

$$J_m(x) = \sqrt{\frac{2}{\pi x}}\left[\cos\left(x - \frac{m\pi}{2} + \frac{\pi}{4}\right)\right.$$
$$\times \sum_{k=0}^{\infty} \frac{(-1)^k}{2^{2k}} \frac{\Gamma(m+2k+1/2}{(2k)!\Gamma(m-2k+1/2)} x^{2k} - \sin\left(x - \frac{m\pi}{2} + \frac{\pi}{4}\right)$$
$$\left.\times \sum_{k=0}^{\infty} \frac{(-1)^k}{2^{2k+1}} \frac{\Gamma(m+2k+3/2)}{(2k+1)!\Gamma(m-2k-1/2)} x^{2k+1}\right] \qquad (93)$$

where Γ denotes the gamma functions. As such, integrands are written in series containing terms of the following form

$$\int_K^{\infty} \frac{A_p \sin(\alpha x + \beta)}{x^p}\, dx \qquad (94)$$

which can be readily evaluated by exploiting sine and cosine integrals and their derivatives if p is a positive integer, or error functions and their derivatives if p is a positive half-integer larger than 1 (15).

When gyromagnetic layers appear in the layered structure, instead of using the vector potential $\boldsymbol{A}$, it is more convenient to express the electric field $\boldsymbol{E}$ and magnetic field $\boldsymbol{H}$ directly in the formulation. This is because the dispersion relation for a gyromagnetic medium together with the associated $\boldsymbol{E}$ and $\boldsymbol{H}$ fields are already known (3), which can be readily used to compose the boundary conditions at the layer interface and the metal patch position. We are still working in the transverse Fourier spectra domain but do not use the point dipole solutions. Thus, as before, by starting from the outermost layer interfaces, we postulate the unknown

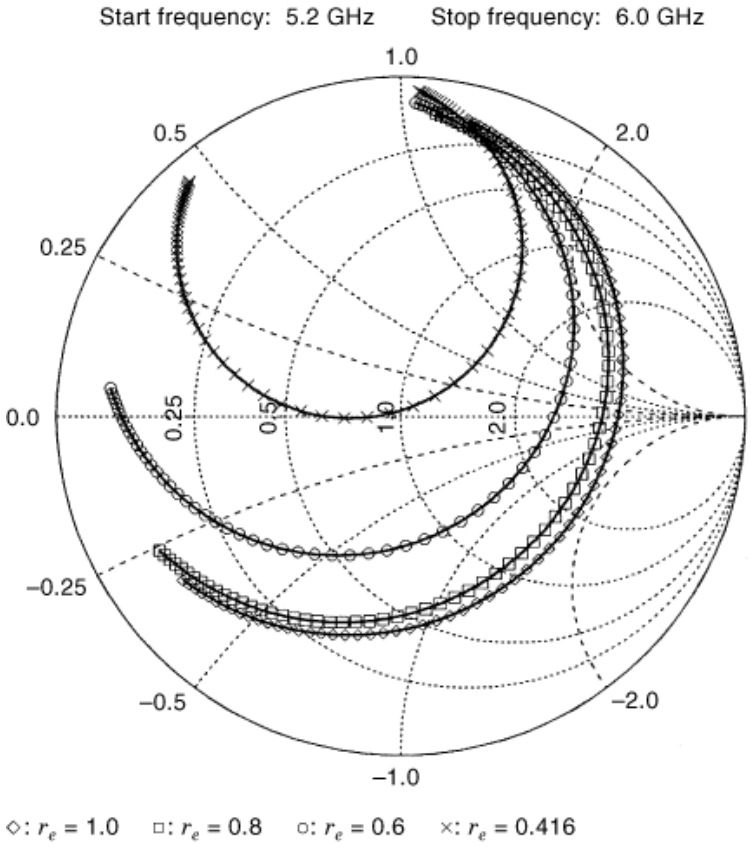

Fig. 10. Input impedance loci of the antenna for several coax feeder positions.

coefficients for $\boldsymbol{E}_t$ and $\boldsymbol{H}_t$ and translate the field components layer after layer until reaching the interface containing the metal patch. For dielectric layers, the field solutions can be expressed in the form of Eqs. (72) and (73) relating $\boldsymbol{E}_t$ and $\boldsymbol{H}_t$ on both sides of the layer. For a gyromagnetic layer, a similar expression is used, except that the propagation constant γ in Eqs. (72) and (73) become nondegenerate; together with the four a, b, c, d coefficients, these propagation constants need to be solved from a quartic dispersion relation (19). This nondegeneracy for wave propagation with respect to different propagation direction and polarization comes from the tensor behavior of the permeability, called Polder tensor (3). In principle, there is no fundamental difference in handling dielectric and magnetic layers, except that more algebraic steps are involved in solving the dispersion relation imposed by the Polder tensor. At the metal patch boundary the discontinuity in $\boldsymbol{H}_t$ gives rise to surface current densities th relates to $\boldsymbol{E}_t$ through Ohm's law and are expressed in the form of an integral equation discussed later.

Numerical Solutions. The dyadic Green's function, $\boldsymbol{G}(\boldsymbol{r}, \boldsymbol{r}')$, is defined as the electric field at location $\boldsymbol{r}$ produced by a unit point dipole located at $\boldsymbol{r}'$. We can solve the current distribution over a microstrip metal patch of negligible thickness deposited on a layered structure backed by a ground plane. Therefore, $\boldsymbol{r}$ and $\boldsymbol{r}'$ are both located at the metal patch, and essentially we have a two-dimensional problem with the third dimension, the z-direction, being absorbed into the Green's function. Thus, we are required to solve the following integral

equation

$$t_e\left[\iint_s \boldsymbol{G}(\rho,\rho').\boldsymbol{J}(\rho')d^2\,\rho' + R_s\boldsymbol{J}(\rho)\right] = \boldsymbol{E}_e(\rho) \qquad (95)$$

where S denotes the metal patch with surface impedance $R_s = (1+j)\sqrt{\omega\mu_o\,2\sigma}$. The first term in Eq. (95) is the electric field returned by the background layered structure the second term relates to the Ohm's current (induction and conduction), and $\boldsymbol{E}_e$ is the electric field generated by an external current. Of special concern, in Eq. (95), t_e results from integration along the z-axis, and hence it defines the effective thickness of the metal patch to be either the skin-depth thickness, $\delta = (2/\mu\omega_0\sigma)^{1/2}$, or the physical thickness of the metal patch, t, whichever is smaller. For a perfect metal patch, $t_e = 0$. Thus, t_e represents the singular behavior of the current distribution exhibiting a delta-function profile in the thickness direction. However, we expect that t_e will not appear in the final expressions evaluating engineering parameters of the antenna, as is the case in Eqs. (96), (98), (99), and (103). In Eq. (95) we have used ρ and ρ' as the two-dimensional position vectors on the metal patch for which the z coordinate is clear.

We denote by $\{\boldsymbol{J}_{mn}(\rho)\}$ a complete orthonormal vector basis for currents on the metal patch. We note that $\{\boldsymbol{J}_{mn}(\rho)\}$ is the regular part of the surface current density, and the singular part is factored out in Eq. (97) as ${t_e}^{-1}$, characterizing, again, the delta-function-like distribution of surface current along the z-direction. Thus, the dimension of $\boldsymbol{J}_{mn}$ is amperes permeter. We apply the Galerkin's method to convert the integral equation [Eq. (95)], into the following matrix form

$$\sum_{m',n'} [B_{mnm'n'}][a_{m'n'}] = [b_{mn}] \qquad (96)$$

where $[\,a_{mn}\,]$ are the unknown coefficients to be solved expressed in terms of the current basis $\{\boldsymbol{J}_{mn}(\rho)\}$,

$$\boldsymbol{J}(\rho) = t_e^{-1}\sum_{mn} a_{mn}\boldsymbol{J}_{mn}(\rho) \qquad (97)$$

and $[\,B_{mnm'n'}\,]$ the matrix elements derived from Eq. (95)

$$B_{mnm'n'} = \iint_S d^2\rho \iint_S d^2\rho'\boldsymbol{J}^*_{mn}(\rho)\cdot\left[\boldsymbol{G}(\rho,\rho') + R_s\boldsymbol{I}\right]\cdot\boldsymbol{J}_{m'n'}(\rho') \qquad (98)$$

where $\boldsymbol{I}$ denotes the identity dyad. The inhomogeneous term of Eq. (96), $[\,b_{mn}\,]$, is associated with current driving given by

$$b_{mn} = \iint_S d^2\rho\boldsymbol{J}^*_{mn}(\rho)\cdot\boldsymbol{E}_e(\rho) = t_e^{-1}\iiint_V d^3\boldsymbol{r}\boldsymbol{E}_{mn}(\boldsymbol{r})\cdot\boldsymbol{J}_e(\boldsymbol{r})^*$$
$$= \iiint_V d^3\boldsymbol{r}\iint_S d^2\rho'\boldsymbol{J}_{mn}(\rho')\cdot\boldsymbol{G}(\boldsymbol{r},\rho')\cdot\boldsymbol{J}_e(\boldsymbol{r})^* \qquad (99)$$

where $\boldsymbol{E}_{mn}$ is the electric field generated by $\boldsymbol{J}_{mn}$, $\boldsymbol{J}_e$ is the driving current density, and integration is over the whole volume, V. In Eq. (99) the reciprocity theorem has been used, which states that a response of a system to a source is unchanged when the source and observer are interchanged (20). The unit drive-current density may be specified as

$$\begin{aligned}\boldsymbol{J_e}(\boldsymbol{\rho}, z) &= \boldsymbol{e}_z\,\delta(x-x_o)\,\delta(y-y_o)\,[S(z)-S(z-d)]/2,\\ &\quad \text{for rectangular patch}\\ &= \boldsymbol{e}_z\,\delta(\rho-\rho_o)\,\delta(\phi-\phi_o)\,[S(z)-S(z-d)]/(2\rho),\\ &\quad \text{for circular patch}\end{aligned} \tag{100}$$

$$\begin{aligned}&\boldsymbol{J}_e\ (\boldsymbol{\rho}, z)\\ &= \boldsymbol{e}_2[S(x-a)-S(x-b)]\delta(y)[S(z)-S(z-d)]/[4(a+b)],\\ &\quad \text{for rectangular patch}\\ &= \boldsymbol{e}_z\,\delta(\rho-R)[S(\phi+\alpha)-S(\phi-\alpha)]\,[S(z)-S(z-d)]/(8\alpha\rho),\\ &\quad \text{for circular patch}\end{aligned} \tag{101}$$

Equations (100) and (101) are for coax and microstrip feeders, respectively, In Eqs. (100) and (101), $S(x)$ denotes the step function and

$$\begin{aligned}S(x) &= 0 \qquad \text{if } x < 0\\ &= 0.5 \qquad \text{if } x = 0\\ &= 1 \qquad \text{if } x > 0\end{aligned} \tag{102}$$

Therefore, assuming unit excitation current, the input impedance is

$$\begin{aligned}Z_{\text{in}} &= -t_e \iint_S d^2\boldsymbol{\rho}\boldsymbol{E}_e^*(\boldsymbol{\rho})\cdot\boldsymbol{J}(\boldsymbol{\rho})\\ &= -\sum_{m,n,m',n'}[b_{mn}]^*[B_{mnm'n'}]^{-1}[b_{m'n'}]\end{aligned} \tag{103}$$

The radiation field associated with a point (Hertzian) dipole located at the air dielectric interface of a microstrip structure is (16)

$$\begin{aligned}\boldsymbol{E}_\theta &= -j\frac{Z_0}{\lambda_0}\cos\phi\ g_\theta\ (\theta)\frac{e^{ik_0r}}{r}\\ \boldsymbol{E}_\phi &= j\frac{Z_0}{\lambda_0}\sin\phi\ g_\phi(\theta)\frac{e^{ik_0r}}{r}\end{aligned} \tag{104}$$

where

$$g_\theta(\theta) = \frac{T\cos\theta}{T - j\epsilon_r\cos\theta\,\cot(Tk_od)} \tag{105}$$

$$g_\theta(\theta) = \frac{\cos\theta}{\cos\theta - jT\cot(Tk_o d)} \tag{106}$$

and

$$T = \sqrt{\epsilon_r - \sin^2\theta} \tag{107}$$

The radiation pattern for a given patch current distribution $\boldsymbol{J}(\rho)$, Eq. (107), is therefore

$$\boldsymbol{E}^{\text{rad}}(\boldsymbol{r}) = -j\frac{\zeta_0}{\lambda_0}e^{\frac{-jk_0 r}{r}}\left[\iint d^2\boldsymbol{\rho}e^{j\boldsymbol{k}\boldsymbol{\rho}}\boldsymbol{J}(\boldsymbol{\rho})\right] \cdot [g_\theta(\theta)\boldsymbol{e}_\phi \times \boldsymbol{e}_z\boldsymbol{e}_\theta + g\phi(\theta)\boldsymbol{e}_\phi\boldsymbol{e}_\phi] \tag{108}$$

where $\zeta_0 = (\eta_0/\epsilon_0)^{1/2}$ and $k_o = 2\pi/\lambda_0 = \omega(\epsilon_0\eta_0)^{1/2}$ are, respectively, the impedance and wavenumber in air.

A convenient current basis can be derived from the intrinsic functions associated with the metal patch geometry (21). We define a set of current potential $\{\psi_{mn}(\rho)\}$ satisfying the two-dimensional Helmholtz equation

$$(\nabla_t^2 + k_{mn}^2)\ \psi_{mn}(\boldsymbol{\rho}) = 0 \tag{109}$$

from which the current basis $\{\boldsymbol{J}_{mn}(\rho)\}$ is defined as

$$\boldsymbol{J}_{mn}(\boldsymbol{\rho}) = \nabla_t\ \psi_{mn}(\boldsymbol{\rho}) \tag{110}$$

The boundary condition imposed on $\{\boldsymbol{J}_{mn}(\rho)\}$ is that the current is not allowed to flow across the metal patch boundary, or, at the patch boundary

$$\boldsymbol{n}\cdot\boldsymbol{J}_{mn} = 0 \tag{111}$$

where **n** denotes the unit outward normal at the metal patch boundary. That is

$$\boldsymbol{n}\cdot\nabla_t\psi_{mn} = 0 \qquad \text{at the patch boundary} \tag{112}$$

Equation (112) determines the eigenvalues k_{mn} in Eq. (109). The current potential can thus be determined, and, for a rectangular patch located at $0 \le x \le L$, $0 \le y \le W$, we have

$$\psi_{mn}(x, y) = (4/LW)\cos(m\pi x/L)\cos(n\pi y/W), \quad m, n = 1, 2, 3, \ldots \tag{113}$$

For a circular patch located at $0 \le \rho \le R$, we have

$$\psi_{mn}(\rho, \phi) = \left[\sqrt{\pi}\beta_{mn}R(1 - \frac{m^2}{\beta_{mn}^2R^2})^{1/2}J_m(\beta_{mn}R)\right]^{-1} J_m(\beta_{mn}\rho)\exp(jm\phi) \tag{114}$$

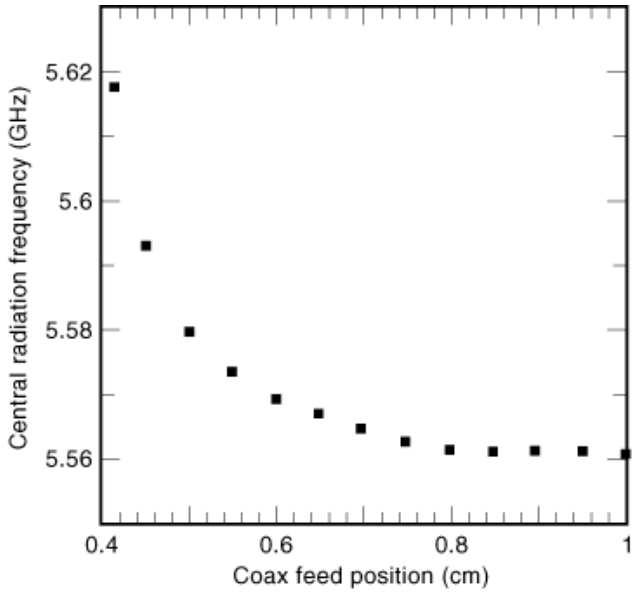

Fig. 11. Calculated radiation frequency as a function of coax feeder position.

and β_{mn} denotes the root of the derivative of the Bessel function, $J_m{}'(x)$

$$J_m'(\beta_{mn}R) = 0 \qquad (115)$$

The advantages of using current potentials are that not only the vector Galerkin equations are converted into a scalar ones, but also most of the integrations can be carried out analytically, including those required to perform inverse transverse Fourier transforms, rendering only one-fold Sommerfeld-type integrals to be evaluated numerically. This is true even in the presence of multiple patches exhibiting close coupling. We note that the current basis introduced in Eq. (110) corresponds to the normal-mode currents appearing in the cavity model of the antenna resonator. Because the basis current is defined as the gradient of a scalar function [the current potential, Eq. (110)], we call it an irrotational current (21).

In the following we present the results of some calculations for circular microstrip patch antennas (15). For rectangular patch antennas, see Ref. 22. The first calculation applies to the published data of a circular antenna characterized by the following parameters (13): $R = 6.75$ cm, $d = 0.1588$ cm, $\epsilon_r = 2.62$, and $\tan \delta = 0.001$. The calculated resonance frequency of the fundamental mode is 0.7936 GHz (15), which compares exactly with the measured value of 0.794 GHz (13). This is contrasted with the calculation for a cavity model presented in the first section, which predicts a resonant frequency of 0.805 GHz (13). The calculated input impedance of the antenna is shown in Ref. 15, which compares nicely with measurements shown as small circles in Fig. 3 (13). Figures 5 and 6 show the calculated radiation pattern of the antenna in the $\phi = 0^\circ$ and $\phi = 90^\circ$ planes, respectively. We note that only copolarized radiations are generated from the fundamental mode excitation; the cross-polarized field cancels out for the two $m = 1$ and $m = -1$ modes at the fundamental resonant frequency.

The second patch antenna geometry considered is a microstrip disk of radius $R = 1$ cm, which is fed by either a coax line or a microstrip line (15). The substrate has of dielectric constant $\epsilon_r = 2.2$, loss tangent $\tan \delta = 0.001$, whose thickness d that varies Figures 7 to 9, assuming $\alpha = 0.2$ rad, show the calculated resonant

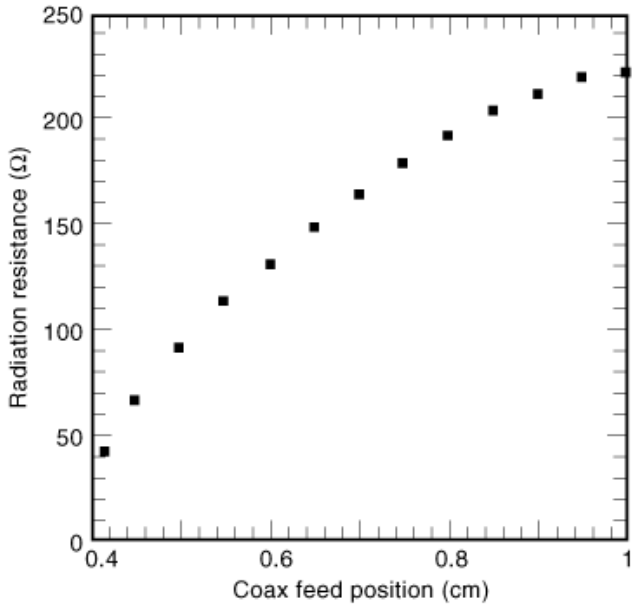

Fig. 12. Calculated radiation resistance as a function of coax feeder position.

frequency, input impedance, and radiation linewidth of the fundamental mode as a function of the substrate thickness, respectively. In Fig. 7 the calculated resonant frequency of the antenna decreases monotonically with the substrate thickness d, indicating that the effective dimension of the patch resonator increases with d, as expected for a leaky cavity. Figure 8 shows that the input impedance of the antenna is relatively a constant, unless d becomes very small, say, smaller than 0.05 cm. In Fig. 9, we see that the radiation bandwidth increases with d, d hence the Q factor of the antenna decreases with d. This finding is consistent with Fig. 7 which exhibit the leaky feature of the antenna patch cavity.

Figure 10 shows the calculated input impedance loci of the above circular antenna of substrate thickness $d = 0.1$ cm fed by a coax line located at $(\rho_0, 0)$. In Fig. 10, the parameter r_e is defined as $r_e = \rho_0/R$, and $r_e = 1.0$, 0.8, 0.6, and 0.416. For each feeder location, the two resonance frequencies shown in Fig. 10 are the resonance frequencies of the probe-inductance in parallel with the detuned patch-resonator, forming a parallel-resonant circuit, and the resonance frequency of the probe-inductance in series with the detuned patch-parallel resonator, forming a series-resonant circuit. The field distribution of the patch at both frequencies shows very little difference, and the patch is operated at the same resonance mode yet more or less detuned from its resonance frequency, which occurs between these two frequencies. It can be seen from Fig. 10 that these resonant frequencies appear only if $0.416 \leq r_e \leq 1$. For $r_e \leq 0.416$, no patch resonance can possibly be excited. Figure 11 shows the calculated radiation frequency as a function of r_e, or ρ_0. It is seen in Fig. 11 that radiation frequency remains roughly constant for $0.6 \leq r_e \leq 1$, which increases rapidly when r_e is further reduced. Figure 12 shows the calculated input resistance as a function of r_e, or ρ_0. From Fig. 12, we see that the input impedance decreases with r_e or ρ_0, and hence it is possible to design 50 Ω input resistance of the antenna by feeding the antenna at $r_e = 0.442$ (or $r_e = 0.488$ for 75 Ω input impedance).

Finally, we consider the interaction between two identical circular microstrip patch antennas excited by microstrip feeders of equal amplitude and phase. Let the antennas be deployed in parallel exhibiting the same parameters considered before: $R = 1$ cm, $d = 0.1$ cm, $\epsilon_r = 2.2$, and the feeder lines having 50 Ω resistance (width 0.312 cm). The separation between the antennas is designated $\boldsymbol{R}_{12}$ measured between their respective

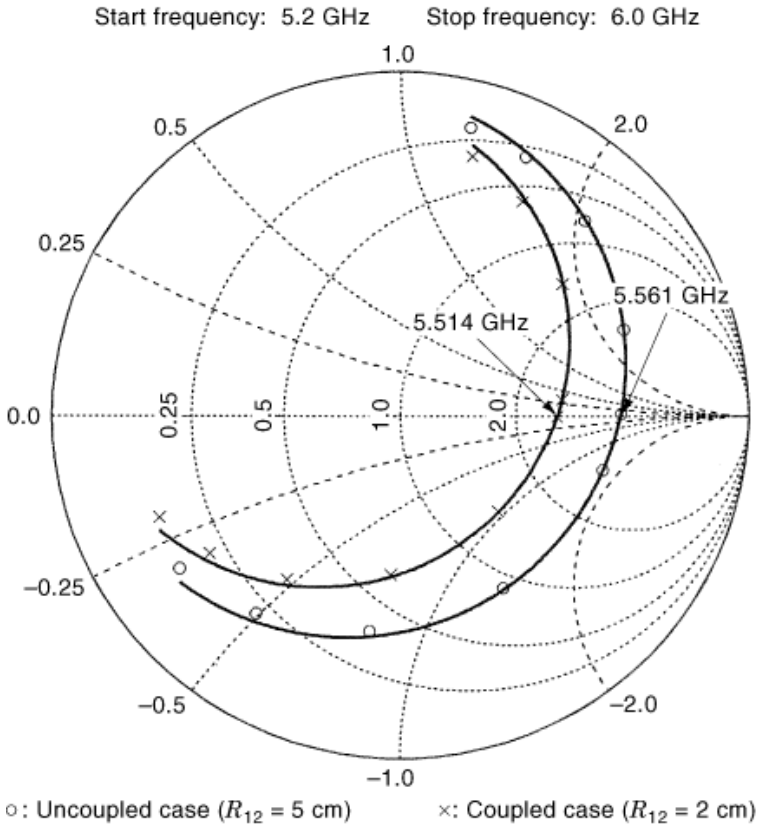

Fig. 13. Calculated and measured input impedance loci of two coupled patch antennas.

centers. Figure 13 shows the calculated and measured input impedance for the coupled case, $\boldsymbol{R}_{12} = 2$ cm (the patches are touching each other), and the uncoupled case, $\boldsymbol{R}_{12} = 5$ cm (the patches are separated by 3 cm at their edges). Measurements were performed with respect to patch antennas fabricated using RT/Duroid 5880 material (Rogers Co., Chandler, AZ). The measured resonant frequencies were 5.514 and 5.561 GHz for the coupled and uncoupled cases, respectively, which compare almost exactly with their calculated values of 5.5137 and 5.5642 GHz. The resonant frequencies of the patches and their input impedance have also been calculated as a function of the patch separation, $\boldsymbol{R}_{12}$. These are shown in Figs. 14 and 15, respectively, with measurements shown as solid squares. From Fig. 14, it is seen that the resonant frequency changes most rapidly when $\boldsymbol{R}_{12}$ is small, say, when $2 \leq \boldsymbol{R}_{12} \leq 3$ cm. Further increase in $\boldsymbol{R}_{12}$ does not change the resonance frequency much. However, the input impedance does show long-range interference between two patch antennas. As shown in Fig. 15 the input impedance is still increasing when the two antennas are separated by 5 cm, although the rate of increase has slowed compared with its initial rate at $R_{12} = 2$ cm.

We conclude that the leaky feature of an antenna cavity can be well characterized by using a full-wave analysis outlined previously. Among many numerical methods, the dyadic Green's function approach might prove to be the simplest one to apply, not only because the analysis is two dimensional, but also because the evaluation of the scalar Galerkin elements involves only onefold Sommerfeld-type integrals. Surface-wave generation is significant for a thick dielectric substrate with large dielectric constant. The coupling between

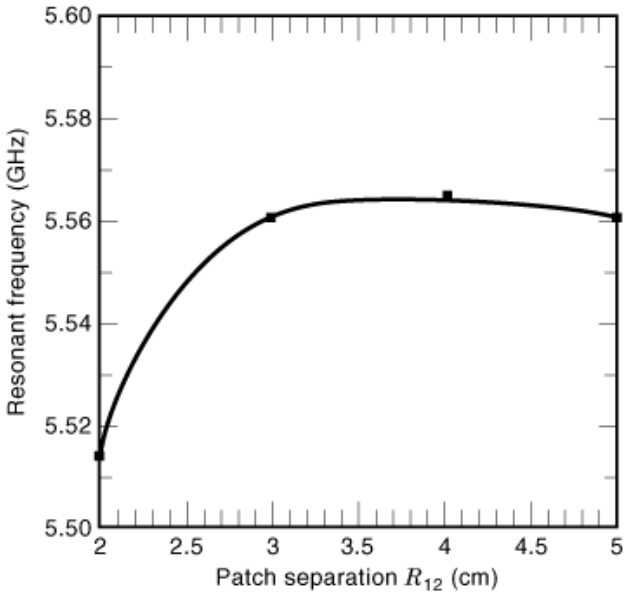

Fig. 14. Calculated and measured resonant frequency of two coupled patch antennas as a function of their separation distance.

microstrip elements is of long-range nature, although the radiation frequency of a patch is less influenced by its neighboring antenna elements.

Recent Developments

Wideband Techniques. A microstrip patch antenna is inherently narrowband, stemming from the cavity model that an electromagnetic resonator confining energy locally in space with little dissipation is necessarily a high-Q, and hence narrowband, device. For a high-Q resonator the generation of surface waves is insignificant. For a thin substrate, this condition amounts to $d/\lambda_0 < 0.07$ for $\epsilon_r = 2.3$ and $d/\lambda_0 < 0.023$ for $\epsilon_r = 10$, as stated previously (10,11). For a microstrip antenna fabricated on a thin substrate the impedance bandwidth is typically 1% to 3%. This is in contrast to the bandwidth of 16% of a half-wave dipole with a radius to length ratio equal to 0.01, and 70% of a medium-length helix operating in the axial mode.

A number of techniques have been proposed to increase the bandwidth of a microstrip patch antenna. These techniques are generally classified into three categories. The first category involves a straightforward approach based on the use of a thick substrate whose dielectric constant is small. The second approach is to design a matching network to enhance the bandwidth (23). The third method uses parasitically coupled elements in a variety of ways to produce closely spaced multiple resonances of the antenna (24,25).

By using a thick substrate whose dielectric constant is considerably different from that of air, surface waves will be generated and inevitably reduce the radiation efficiency and introduce interference between array elements. To resolve this problem, air cavities or holes may be introduced with the substrate to effectively reduce the dielectric constant of the patch. For example, 26 machined closely spaced holes in a Duroid substrate underneath a microstrip patch to lower the effective dielectric constant of the antenna. Using a micromachining technique, Zheng et al. measured a 12.8% impedance bandwidth on cavity-backed microstrip patch antennas fabricated on silicon wafers (27).

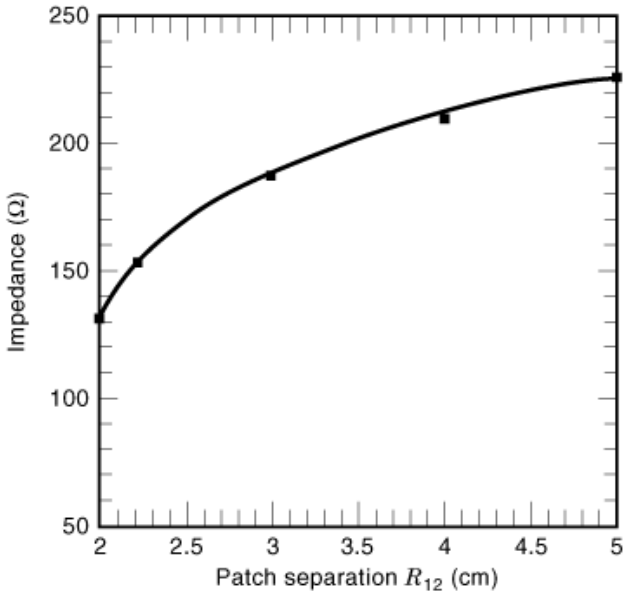

Fig. 15. Calculated and measured input impedance at resonance of two coupled patch antennas as a function of their separation distance.

The bandwidth of the antenna is primarily determined by the rate of transition that the imaginary part of the impedance changes sign at resonance, as discussed previously. Thus, it is possible to introduce a cancellation mechanism on the input inductance so as to smooth the impedance variation. For example, the inductance associated with the long wire-lead of the coax probe will limit the bandwidth to $<$10% for a thick substrate. By etching a small circular slot around the probe on the patch, capacitance is introduced that cancels the probe inductance to produce a bandwidth of 16% (28). Recently, with the use of a U-shaped slot, a substantial increase in bandwidth (32%) has been demonstrated (29). Alternatively, an L-shaped probewire has been shown to result a bandwidth of 28 percent (30).

The third method to achieving broadband operation is to couple the microstrip patch antenna parasitically with other dielectric resonators characterized by approximately the same resonant frequency of the patch. For an isolated patch the resonant frequency is determined by its lateral dimension. In the presence of fringe fields at the patch periphery, however, the boundary of the antenna is neither sharply nor rigidly defined, leading to a slightly larger effective dimension of the patch, as described by Eqs. (2) and (5) for rectangular and circular microstrip patches, respectively. Thus, in contrast to a metal cavity, patch antennas have soft boundaries, which in turn give rise to finite bandwidth in radiation: the softer the boundary, the wider the bandwidth. For this reason, a patch antenna fabricated on a thick substrate will show a wide bandwidth. Similarly, when coupled together, many soft-boundary microstrip resonators or patches, the overall radiation bandwidth is consequently enlarged.

The disadvantage of using a thick substrate is that, besides its cost, surface waves may be generated in the substrate so as to reduce the antenna feeding efficiency. By using multiple electromagnetically coupled patches this disadvantage can be overcome. Electromagnetically coupled patches can be deployed either side by side (laterally coupled geometry) or layer by layer (vertically coupled geometry). For laterally coupled patches, the antenna size will increase considerably, ultimately restricting its usage large-array applications (31).

The two-layer electromagnetically coupled patch antenna consisting of a driven (feeder) patch in the bottom and a parasitic (radiating) patch on the top has been investigated by several authors. For circular (32), equitriangular (33), and rectangular (34) patches, experimental results have shown an enhanced gain and impedance bandwidth with low cross-polarization levels as compared with the conventional single-layer microstrip antenna. Actually, like a Yogi antenna, the gain of a stacked antenna can be increased to above 20 dBi at any scan angle if the thickness of the substrate and multiple superstrate layers is chosen pperly (35). Therefore, using stacked parasitic elements in microstrip arrays could improve the overall array performance, offering a higher gain and broad bandwidth, meeting with the same array design criteria of a conventional single-layer microstrip array but with fewer array elements.

Size Reduction. Microstrip antennas have a number of advantages over conventional antennas, namely, small size, light weight, low production cost, and natural conformity. For many applications, however, for example, hand-held mobile communications systems, half-wave microstrip antennas etched on a low-cost dielectric substrate are still too large to be accommodated on a portable phone. A well-known method of reducing the size of a half-wave patch to a quarter wave is to introduce an electric-shorting wall at one of the radiating edges. Hiraswa and Haneishi (36) have shown that the length of the patch can be made sufficiently shorter than a quarter wave by replacing the shorting wall with a shorting pin at the corner of the patch. Recently, Wong and Lin have shown that by replacing the shorting pin with a chip resistor of low resistance, antenna size can be further reduced, with an additional increase in bandwidth (37).

The other approach to reduce antenna size is to use a meandered geometry of the patch antenna (36). By meandering the patch, the effective electrical length is larger than the physical length. Consequently, the resonant frequency of the meandered antenna can be much lower than that of a conventional design with the same physical length (38).

Finally, we note that not only is it possible to achieve high gain for printed circuit antennas, it is also feasible to shape the radiation pattern in a prescribed manner. Some very interesting phenomena, such as radiation into the horizon, radiation pattern monodirectionality, and azimuthal-dependent radiation have been found possible (39). Furthermore, laterally coupled patches can serve as adaptive array antennas, because the phase of radiation from a parasitic element can be adjusted via a varactor diode inserted at some feeding position (40). The important feature of an adaptive array antenna is that it can provide beam steering as required by many communications and traffic control systems (41).

BIBLIOGRAPHY

1. A. Sommerfeld, *Partial Differential Equations*, New York: Academic Press, 1962.
2. J. R. James P. S. Hall (eds.), *Handbook of Microstrip Antennas*, Vols. **1** and **2**, London: Peter Peregrinus, 1989.
3. H. How, T.-M. Fang, C. Vittoria, Intrinsic modes of radiation in ferrite patch antennas, *IEEE Trans. Microw. Theory Tech.*, **MTT-42**: 988, 1994.
4. E. O. Hammerstad, Equations for microstrip circuit design, *Proc. 5th Eur. Microstrip Conf.*, Hamburg, September, 1975, pp. 268–272.
5. M. V. Schneider, Microstrip lines for microwave integrated circuits, *Bell System Tech. J.*, **48**: 1421–1444, 1969.

6. L. C. Shen, Resonant frequency of circular disc, printed circuit antenna, *IEEE Trans. Antennas Propagat.*, **AP-25**: 596, 1977.
7. J. A. Stratton, *Electromagnetic Theory*, New York: McGraw-Hill, 1941.
8. R. S. Elliott, *Antenna Theory and Design*, Englewood Cliffs, NJ: Prentice-Hall, 1981.
9. A. G. Derneryd, Microsip array antenna, *Proc. 6th Eur. Microw. Conf.*, 1976, pp. 339–343.
10. J. R. James A. Henderson, High-frequency behavior of microstrip open-circuit terminations, *IEE J. Microw. Opt. Acoust.* **3**: 205–218, 1979.
11. C. Wood, Analysis of microstrip circular patch antennas, *IEE Proc.*, **128** (H): 69–76, 1981.
12. S. B. A. Fonseca A. J. Giarola, microstrip disk antennas, part I: Efficiency of space wave launching, *IEEE Trans. Antennas Propagat.*, **AP-32:** 561–567, 1984.
13. Y. T. Lo, D. Solomon, W. F. Richards, Theory and experiment on microstrip antennas, *IEEE Trans. Antennas Propagat.*, **AP-27**: 137–145, 1979.
14. R. C. Booton, Jr., *Computational Method for Electromagnetics and Microwaves*, New York: Wiley, 1992.
15. H. How C. Vittoria, Directions for the next generation of MMIC devices and systems, in N. K. Das and H. L. Bertoni, (eds.), *Computer Aided Design Tools for Microstrip Circuitries*, New York: Plenum, 1997, pp. 399–406.
16. J. R. Mosig, R. C. Hall, F. E. Gardiol, Numerical analysis of microstrip patch antennas, in *Handbook of Microstrip Antennas*, J. R. James and P. S. Hall, (eds.), London: Peter Peregrinus, 1989, pp. 393–453.
17. J. D. Jackson, *Classical Electrodynamics*, New York: Wiley, 1975.
18. S. Y. Liao, *Microwave Devices and Circuits*, Englewood Cliffs, NJ: Prentice-Hall, 1985.
19. C. Vittoria, *Microwave Properties of Magnetic Films*, Singapore: World Scientific, 1993.
20. R. F. Harrington, *Time Harmonic Electromagnetic Fields*, New York: McGraw-Hill, 1961.
21. H. How C. Vittoria, Radiation modes in dielectric circular patch antennas, *IEEE Trans. Microw. Theory Tech.*, **MTT-42**: 1939, 1994.
22. D. M. Pozar, Input impedance and mutual coupling of rectangular microstrip antennas, *IEEE Trans. Antennas Propag.*, **AP-30**: 1191, 1982.
23. H. An, K. J. C. Nauwelaers, A. R. Van de Capelle, Broadband microstrip antenna design with the simplified real frequency technique, *IEEE Trans. Antennas Propag.*, **AP-42**: 129–136, 1994.
24. R. Q. Lee, K. F. Lee, J. Bobinchak, Characteristics of a two layer electromagnetically coupled rectangular patch antenna, *Electron. Lett.*, **23**: 1070–1072, 1987.
25. C. K. Aanandan, P. Mohanan, K. G. Nair, Broadband Gap-Coupled Microstrip Antenna, *IEEE Trans. Antennas Propag.* **AP-38**: 1581–1586, 1990.
26. G. P. Gauthier, A. Courtay, G. M. Rebeiz, Microstrip antenna on synthesized low-dielectric constant substrates, *IEEE Trans. Antennas Propag.*, **AP-45**: 1310–1314, 1997.
27. M. Zheng, et al., Broadband microstrip patch antennas on micromachined silicon substrates, *Electron. Lett.*, **34** (1): 3–4, 1998.
28. P. S. Hall, Probe compensation in thick microstrip patches, *Electron. Lett.*, **23**: 606–607, 1987.
29. K. F. Lee, et al., Experimental and simulation studies of coaxially fed U-slot rectangular patch antenna, *IEE Proc. Microw. Antennas Propag.*, **144**: 354–358, 1997.
30. K. M. Luk, et al., Broadband microstrip patch antenna, *Electronics Lett.*, **34** (15): 1442–1443, 1998.
31. S. Dey R. Mittra, A compact broadband microstrip antenna, *Microw. Opt. Technol. Lett.*, **11** (6): 295–297, 1996.
32. A. Sabban, A new broadband stacked two-layer microstrip antenna, *IEEE AP-S Int. Symp. Dig.*, 63–66, 1983.
33. P. S. Bhatnagar, et al., Experimental study on stacked triangular microstrip antennas, *Electron. Lett.*, **22**: 864–865, 1986.
34. R. Q. Lee K. F. Lee, Experimental study of the two-layer electromagnetically coupled rectangular patch antenna, *IEEE Trans. Antennas Propag.*, **AP-38**: 1298–1302, 1990.
35. H. Y. Yang G. N. Alexopoulos, Gain enhancement methods for printed circuit antennas through multiple superstrates, *IEEE Trans. Antennas Propag.*, **AP-35**: 860–863, 1987.
36. K. Hiraswa M. Haneishi, *Analysis, Design, and Measurement of Small and Low-Profile Antennas*, London: Artech House, 1992, Ch. 5.
37. K. Wang Y. Lin, Small broadband rectangular microstrip antenna with chip-resistor loading, *Electron. Lett.*, **33** (19): 1593–1594, 1997.
38. S. Dey R. Mitttra, Compact microstrip patch antenna, *Microw. Opti. Technol. Lett.*, **13 (1)**: 12–14, 1996.

39. H. Y. Yang N. G. Alexopoulos, Generation of nearly hemispherical and high gain azimuthal symmetric patterns with printed circuit antennas, *IEEE Trans. Antennas Propag.*, **35**: 972–977, 1987.
40. D. Cailleu, N. Haese, P. A. Rolland, Microstrip adaptice array antenna, *Electron. Lett.* **32** (14): 1246–1247, 1996.
41. R. J. Dinger, A planar version of a 4.0 GHz reactively steered adaptive array, *IEEE Trans. Antennas Propag.*, **34**: 427–431, 1986.

HOTON HOW
ElectroMagnetic Applications
CARMINE VITTORIA
Northeastern University